Structure and reactivity of sodium aluminate complexes in alkaline solutions

Emily T. Nienhuis [a], Maxime Pouvreau [a,b], Trent R. Graham [a], Micah P. Prange [a], Katharine Page [d,e], John S. Loring [a], Andrew G. Stack [f], Aurora E. Clark [b], Gregory K. Schenter [a], Kevin M. Rosso [a], Carolyn I. Pearce [a,c], Hsiu-Wen Wang [f,*]

[a] Pacific Northwest National Laboratory, Richland, WA 99352, United States
[b] Department of Chemistry, Washington State University, Pullman, WA 99164, United States
[c] Department of Crop and Soil Sciences, Washington State University, Pullman, WA 99164, United States
[d] Department of Materials Science and Engineering, The University of Tennessee, Knoxville, TN 37996, United States
[e] Neutron Scattering Division, Oak Ridge National Laboratory, Oak Ridge, TN 37831, United States
[f] Chemical Sciences Division, Oak Ridge National Laboratory, Oak Ridge, TN 37831, United States

ARTICLE INFO

ABSTRACT

The underlying mechanism by which tetrahedrally-coordinated aluminate solution species react to precipitate octahedrally-coordinated Al^{3+} in gibbsite is unknown. Sodium aluminate solutions provide the opportunity to investigate the role of ion speciation and local structure in the reaction, as the solution metastability can be controlled by varying ratio of excess NaOD to Al^{3+}. Here, capitalizing on this tunable precipitation behavior, aluminate speciation was investigated through a combination of Raman, infrared, and NMR spectroscopies, together with geometrical fitting of neutron and X-ray radial distribution functions. These techniques reveal a mixture of monomeric $Al(OD)_4^-$ and dimeric $Al_2O(OD)_6^{2-}$ in all compositions, but solutions avoiding precipitation for extended timescales (i.e. months to years) show an increased dimeric $Al_2O(OD)_6^{2-}$ population formed at the expense of the $Al(OD)_4^-$ monomer. Conversion between these species, as well the potential for further oligomerization and formation of larger prenucleation species is driven by the hydrogen/deuterium bonding (H/D-bonding) and proton/deuteron transfer reactions. Changes within the local environment around the aluminate anions, including solvation and the presence of solvent-shared ion pairs or contact ion pairs, will consequently govern the reactivity of these aluminate species to either promote or inhibit precipitation.

1. Introduction

A complete understanding of the phase equilibria of alkaline sodium aluminate solutions in the $Na_2O-Al_2O_3-H_2O$ ternary system is necessary to accurately predict the precipitation and dissolution of aluminum (Al^{3+}) (oxy)hydroxides, such as gibbsite ($Al(OH)_3$), during the Bayer process, in which bauxite ore is converted to alumina (Al_2O_3) to produce metallic aluminum [1]. Bauxite ore is dissolved in hot concentrated sodium hydroxide (NaOH), then the solution is cooled to precipitate Al^{3+} as gibbsite, which is further refined to obtain alumina (Al_2O_3) [2]. This slow and inefficient process is complicated by the presence of other dissolved species, such as iron oxides, aluminosilicates, and organic matter [2].

Very similar chemical conditions define the composition of the voluminous radioactive wastes from nuclear weapons production that are currently stored at United States Department of Energy legacy nuclear sites, such as the Hanford site in Washington State [3]. These complex waste materials are dominated by molar concentrations of sodium salts of aluminate ($Al(OH)_4^-$) nitrate (NO_3^-), nitrite (NO_2^-), and hydroxide (OH^-). Al^{3+} is present due to the chemical stripping of Al-clad defense fuels and the use of aluminum nitrate to increase ionic strength in certain reprocessing schemes. The precipitation and aggregation behavior of Al^{3+}-bearing species in this waste is difficult to predict due to the low water activity, high alkalinity, variable composition, and the presence of ionizing radiation [3]. Waste processing for safe long-term storage is estimated to take > 50 years and >$235 billion dollars using existing technologies [4]. Thus, improving understanding of molecular-scale factors controlling chemical transformations and

reactivity in the Na_2O-Al_2O_3-H_2O ternary system could be transformative.

In highly alkaline sodium aluminate solutions, Al^{3+} speciates primarily as $Al(OH)_4^-$ but the impact of this speciation on reactivity and precipitation remains unclear [5]. These solutions can be supersaturated with respect to gibbsite and, at higher NaOH concentration, sodium aluminate salts, such as monosodium aluminate hydrate ($Na_2[Al_2O_3(OH)_2]\cdot1.5H_2O$). Supersaturated solutions at fixed $[Al^{3+}]_{tot}$ but changing $[NaOH]_{tot}$ show complex nucleation behavior, attributable to oligomeric precursors and complex liquid dynamics, which can lead to the formation of amorphous gels, or to direct bulk crystal precipitation [5]. The important role of limited water activity at fixed $[M^+]_{tot}/[Al^{3+}]_{tot}$ and/or the nature of the cation (M^+ = Li^+, Na^+, K^+, Rb^+, and Cs^+) on nucleation has begun to emerge, suggesting a direct link to metastability with respect to precipitation [6,7].

^{27}Al nuclear magnetic resonance (NMR), Raman, and infrared (IR) spectroscopies all indicate that at $[Al^{3+}]_{tot} <$ ~0.5 m, Al^{3+} is predominantly present as the tetrahedrally-coordinated aluminate monomer, $Al(OH)_4^-$ [8]. As the concentration of $[MOH]_{tot}$ and $[Al^{3+}]_{tot}$ is increased, an additional solution species is formed, as evidenced by the emergence of two additional modes on both sides of the $Al(OH)_4^-$ band in the Raman spectra of these solutions. Through comparison with the Raman spectrum of crystalline potassium aluminate salt $K_2Al_2O(OH)_6$ and theoretical ab initio molecular dynamics (AIMD) calculations, these modes have been attributed to formation of the μ_2-oxo bridged aluminate dimer, $Al_2O(OH)_6^{2-}$, also comprised of tetrahedrally coordinated Al^{3+} [9–11]. The existence of a pentacoordinate di-μ_2-hydroxo aluminate dimer, $Al_2(OH)_8^{2-}$, has also been predicted by AIMD [11,12]. Standard notation of μ_2 represents bridging oxygen atoms between two Al^{3+}, and hence μ_2-oxo and μ_2-hydroxo are bridging oxygen and hydroxyl sites present in the two dimers. Compared to the μ_2-oxo $Al_2O(OH)_6^{2-}$ dimer, the di-μ_2-hydroxo $Al_2(OH)_8^{2-}$ dimer is kinetically easier to form, but its presence cannot be directly identified by Raman/IR because its major vibrational signatures are overlapped with the either $Al(OH)_4^-$ band (in Raman) or with $Al_2O(OH)_6^{2-}$ bands (in IR) [11,12]. Although octahedrally-coordinated $Al(OH)_6^{3-}$ in solution has been reported based on ^{27}Al NMR spectroscopy [13], this observation has not been reproduced in studies spanning multiple independent investigators, e.g., [14,15]. Instead ^{27}Al NMR spectroscopy data show that tetrahedrally-coordinated species dominate in alkaline conditions [15–17], consistent with the Raman and FTIR observations.

Nucleation and growth of gibbsite from these solutions thus necessitates Al^{3+} coordination changes from tetrahedral in solution to octahedral in the solid. Although yet to be confirmed, short-lived intermediate species (e.g., 5-coordinated Al^{3+}) could be expected to be necessary for the transformation. The possible facilitation of Al^{3+} coordination change via aluminate polymerization as a precursor step is also unknown. However, in solutions with high $[MOH]_{tot}$ and $[Al^{3+}]_{tot}$ concentrations, where there is insufficient water for complete solvation of all ions present, recent work points to the importance of a resulting extended ion-water network with loosely packed ions connected by hydrogen-bonding (H-bonding), contact ion pairs (CIP), and solvent separated ion pairs (SSIP) [15,18,19]. Systematic studies focused on understanding the role of H-bonding at limited water activity on metastability with respect to precipitation are needed.

To this end, the present study examines a series of supersaturated solutions at fixed $[Al^{3+}]_{tot}$ with variable concentrations of $[NaOD]_{tot}$. These solutions exhibit a range of precipitation behaviors, allowing the role of local aluminate speciation in promoting, or hindering, the precipitation of Al^{3+}-bearing solids to be evaluated. In addition to characterization using Raman, IR, and NMR spectroscopies, we probed aluminate speciation and local solution structure using neutron and X-ray radial distribution function (RDF) analyses with data interpretation supported by AIMD simulations. By linking aluminate speciation to solution-phase reactions, we show that hydrogen (deuterium) bonding (H/D-bonding), and proton (deuterium) transfer motions, are the primary processes that determine solution structure in these concentrated alkaline aluminate systems.

2. Methods

2.1. Materials and solutions

Deuterated sodium aluminate solutions were generated by quantitative dissolution of degreased Al wire (99.999% grade) in concentrated stock NaOD solutions (40 wt%), with selective D_2O addition or removal (by evaporation at elevated temperatures) as needed to achieve the desired $[Na^+]_{tot}$ and $[Al^{3+}]_{tot}$ concentrations listed in Table 1. Chemical information and details of the solution preparation are provided in the Supplementary Material, section 1.

The dissolution/reaction of Al wires can be expressed as simply: $xAl_{(s)} + yNaOD_{(aq)} + 3xD_2O_{(aq)} \rightarrow x\ NaAl(OD)_4\ _{(aq)} + (y-x)$ $NaOD_{(aq)} + (3x/2)D_{2(g)}$. In this expression, Al^{3+} is assumed to be the aluminate monomer $Al(OD)_4^-$. The variable denoted $(y-x)$ defines the excess amount of $[NaOD]_{ex}$ (i.e., free Na^+ and OD^- species) that is not consumed by $Al(OD)_4^-$ formation (in a 1:1 ratio of Na^+ and $Al(OD)_4^-$), and its concentration is subject to change with the formation of dimer or polynuclear aluminate complexes. For instance, if the primarily speciation of Al^{3+} is μ_2-oxo $Al_2O(OD)_6^{2-}$ dimer, the dissolution/reaction can then be written as: $xAl_{(s)} +$ $yNaOD_{(aq)} + 3xD_2O_{(aq)} \rightarrow (x/2)Na_2Al_2O(OD)_{6(aq)} + (y-x)NaOD_{(aq)} + (3-x/2)D_{2(g)} + (x/2)D_2O_{(aq)}$. Here, and throughout the rest of the article, we abbreviated the solution series as s0.1, s1, and s2 for the three sodium aluminate solutions with the $Na^+_{(ex)}/Al^{3+}$ mole ratio of ~0.1, 1.0 and 2.1, respectively (Table 1). Note that these three solutions all have ~9 m $[Al^{3+}]_{tot}$ concentration, and they differ by the concentration of $[Na^+]_{tot}$ and $[OD^-]_{ex}$.

Table 1

Composition of the deuterated sodium aluminate solutions. Deuterated solutions are essential for neutron RDF studies due to the large incoherent scattering lengths of H atoms.

	s0.1	*s1*	*s2*
solute & solvent (moles)[a]			
Na^+	9.91	17.70	29.58
Al^{3+}	9.01	8.69	9.53
OD^-	36.95	43.77	58.19
D_2O	55.51	55.51	55.51
Total	111.38	125.67	152.82
speciation (molal, m)[a]			
x: $NaAl(OD)_4$	9.01	8.69	9.53
y-x: NaOD (excess)	0.90	9.01	20.05
ratio			
$(y$-$x)/x$: $Na^+_{(ex)}/Al^{3+}$	0.1	1.0	2.1
$D_2O/$ $Na^+_{(total)}$	5.6	3.1	1.9
molar mass (M_m; g/mole)	20.17	20.21	20.25
density (d; g/cm^3)[b]	1.55	1.61	1.70
molecular no. density (ρ_m; #/Å^3)[c]	0.046	0.048	0.051

a. Calculations are performed consistently on the basis of 55.51 mol of D_2O. Here, monomer speciation balance is assumed, i.e. no water molecules are formed via condensation of $Al(OD)_4^-$ into $Al_2O(OD)_6^{2-}$.

b. Mass density is obtained based on density data in [20] with a linear regression for the estimation of densities in the studied solutions. Atomic weights by different isotopes are considered in the density estimations.

c. Molecular number density is calculated according to $\rho_m = (N_A d/M_m) \times 10^{-24}$, where N_A is the Avogadro constant, M_m is solution's molar mass, d is density, and 10^{-24} is the unit conversion factor from cm^{-3} to Å^{-3}. To put ρ_m value in perspective, ρ_m of bulk water (H_2O or D_2O) is 0.0333 (Å^{-3}).

2.2. Raman spectroscopy

Raman spectroscopy was performed using a Horiba LabRam HR spectrometer with a Nikon Ti-E inverted microscope using a 632.81 nm continuous laser light source focused through a 40x microscope objective. Spectra were collected between a range of 100–4000 cm^{-1} with a resolution of 1 cm^{-1}. For each sample, ten spectra were collected with a 30 sec exposure time and then averaged. The observed Raman bands are analyzed through fitting the background subtracted Raman spectra with Voigt line shapes using Fityk [21] software. Raman spectra were collected on the same day the deuterated solutions were prepared. See Supplementary Material, section 2 for plots of the whole spectral range.

2.3. Fourier transform infrared spectroscopy

FTIR spectroscopy was performed on a Bruker Vertex 80v with both Mid-IR and Far-IR detectors and beamsplitters and equipped with a Harrick DiaMaxATR single reflection diamond ATR cell. Diamond has excellent chemical compatibility with highly alkaline solutions. Background Mid- and Far-IR spectra were of the empty cell under the vacuum ($\sim$10^{-3} torr) of the spectrometer. Sample IR spectra were of solutions loaded directly onto the ATR crystal. A cover with a rubber gasket was clamped over the solutions to keep them at atmospheric pressure while the spectrometer sample chamber was evacuated. Spectra were collected on the same day the solutions were prepared. Mid-IR spectra between 4000 and 380 cm^{-1} were an average of 512 scans at a resolution of 4 cm^{-1}; Far-IR spectra between 500 and 30 cm^{-1} were an average of 1024 scans also at a 4 cm^{-1} resolution. See Supplementary Material, section 3, for plots of the whole spectral range.

2.4. Nuclear magnetic resonance spectroscopy

NMR spectroscopy was performed on a 11.7467 T NMR spectrometer (Agilent/Varian). At 11.7467 T, the Larmor frequencies of ^{27}Al, ^{23}Na and ^{1}H are 130.318, 132.294, and 500.130 MHz. All NMR spectra were collected at a temperature of 20 °C. Detailed statements describing the experimental parameters for the acquisition of ^{27}Al, ^{23}Na, and ^{1}H pulsed field gradient NMR spectra are given in the Supplementary Material, section 4.

2.5. Neutron and X-ray total scattering and radial distribution function measurements

Neutron total scattering data was collected at the NOMAD beamline at the Spallation Neutron Source (SNS) at Oak Ridge National Laboratory [22]. A double-walled vessel, incorporating commercially-available 5 mm diameter Wilmad fused quartz NMR tubes, polytetrafluoroethylene (PTFE) liners, and PTFE Swage-lok seals, was used as the sample cell [23]. Approximately 3 mL of solution was loaded into each sample cell and sealed in an Ar environment at ambient pressure. The sample vessels were mounted vertically in the NOMAD linear sample changer and aligned in the neutron beam. In this setup, a bracket translates a series of samples into the neutron beam cross section, with an argon cryostream fixed below the aligned sample position. A total of two hours of data was collected for each solution at 300 K. Two hours of data was also collected for an empty cell assembly, to be used for background subtraction. The double-walled sample cell assembly was found to be undamaged up to a period 3 + years (the period transpired at the time of writing this manuscript since loading the samples), allowing for *in situ* or aging studies. The data is absolutely normalized with respect to the composition and density of each solution sample (Table 1). The normalized scattering structure factor datasets, S(Q), were transformed to radial distribution

function datasets, RDF g(r), using the specific IDL codes developed for the NOMAD instrument [22]. RDF patterns were calculated via Fourier transformation of the S(Q) data utilizing a Q$_{max}$ of 40 Å^{-1} and a Lorch modification function was applied to smooth data.

Synchrotron X-ray total scattering data was collected at the 11-ID-B beamline at the Advanced Photon Source (APS) at Argonne National Laboratory. Samples were measured in transmission mode at room temperature using a Perkin Elmer amorphous silicon image plate detector [24], a beam size of 0.5 mm × 0.5 mm, an incident photon energy of 58.6 keV, a wavelength of 0.2115 Å, a sample to detector distance of $\sim$175 mm, and a total measurement time of approximately 5 min per sample. The solution samples were loaded into 2 mm polyimide capillaries in an Ar controlled atmosphere and sealed with epoxy. Data for an empty polyimide container was also collected. Solutions studied here were found to breach containment or deform the polyimide tubing if left for a period of a week or more. All the X-ray data were measured as mail-in samples and thus the unstable s0.1 solution (for which precipitation occurred within a 24-hour period) was not measured. The data is absolutely normalized with respect to the composition and density of each sample (Table 1), and X-ray RDF patterns were calculated via Fourier transformation of the S(Q) data utilizing a Q$_{max}$ of 20 Å^{-1}. For more data reduction details, see the Supplementary Material, section 5.

2.6. Ab initio molecular dynamics simulation

Five different hydrated species were simulated, with the following solute ions placed in periodic cubic boxes ($\sim$14 Å) and solvated by 83–92 H$_2$O (depending on the size of the solute): the Al(OH)$_4^-$ monomer, di-μ_2-hydroxo Al$_2$(OH)$_8^{2-}$ dimer, μ_2-oxo Al$_2$O(OH)$_6^{2-}$ dimer, OH$^-$, and Na$^+$. The volume of the boxes was pre-equilibrated within the *NPT*-ensemble (P = 1 bar, T = 300 K) using classical molecular dynamics (CMD). For the OH$^-$ and Na$^+$ solvation structure, potential models by Joung et al. [25] and Balbuena et al. [26] were adopted, respectively. For the three aluminate ions, in-house force field parameters developed from previous work [12] were used. AIMD simulations were then performed using the CP2K software [27] in the *NVT* ensemble (T = 300 K), with simulation times of 30–40 ps including a production stage of at least 20 ps, and a time step of 0.5 fs. The revised version of the PBE functional (RPBE) by Hammer et al. [28] was used within with the empirical dispersion corrections of Grimme et al. [29]. The Gaussian and plane wave (GPW) scheme [30] was employed with Goedecker-Teter-Hutter pseudopotentials, a plane wave cutoff of 350 Ry (600 Ry for the Na$^+_{(aq)}$ system), and a double-zeta basis set with a single set of polarization functions (DZVP-MOLOPT-SR-GTH [31]). These MOLOPT basis sets are optimized for condensed phase calculations.

Snapshots were extracted every 1000 steps from the trajectories at equilibrium to compute RDF curves. To compute all the pair-wise correlations from the AIMD simulations, we employed the RDF analysis menu in the DISCUS suite [32] software package, and simply substituted D for H atom sites. RDFs were obtained from the average of $\sim$100 configurations within each trajectory, and small isotropic thermal displacement factors (U$_{iso}$) were applied and constrained to be equal for all atoms of the same type (U$_{iso}$:Al = 0.005 Å^2; U$_{iso}$:O = 0.010 Å^2; U$_{iso}$:D = 0.015 Å^2; U$_{iso}$:Na = 0. 005 Å^2). The resulting partial and total RDFs are all self-normalized and scaled by their corresponding neutron- or X-ray-weighted scattering factors to produce RDFs comparable to the experiment. Corrections for Q$_{max}$ terminations and instrumental parameters were not applied. As mentioned in the Supplementary Material, section 5, experimental Q$_{max}$ values determine Δr resolution in the RDF data, and corrections for this termination effect are not needed as atom–atom correlations in these solution samples are

sufficiently disordered that Q_{max} has negligible effect on RDF peak widths. The effect of instrumental parameters is also not considered, as the geometric modeling only focuses upon the local (<5 Å) coordination features.

3. Results & discussion

3.1. Stability and nucleation behavior of sodium aluminate solutions

The phase diagram for sodium aluminate solutions (Fig. 1) is marked with three metastability zones where supersaturated sodium aluminate solutions experience different induction times and pathways for nucleation/crystallization. The grey square boundary at the top-right corner of the diagram outlines the approximate "water-in-salt" concentration region, where there is insufficient D$_2$O to fully solvate all ions in the system, necessitating shared hydration shells. The three solutions investigated herein have a total Al^{3+} concentration of ~9 m and are labelled s0.1, s1 and s2 according to their respective, approximate Na$^+_{(ex)}$/Al^{3+} mole ratios. The s0.1 solution with a low Na$^+_{(ex)}$/Al^{3+} mole ratio precipitates gibbsite within 24 h. As the [Na$^+$]$_{tot}$ is increased, the solution at composition s1 is extremely stable and maintains a supersaturated state without crystallization for years [5]. Beyond this, the solution at composition s2 forms a semi-crystalline gel state after 3–6 months [5,7].

3.2. Aluminate speciation from vibrational spectroscopy

Vibrational spectroscopies (Raman and FTIR) have been used to resolve distinct spectroscopic signatures of the Al(OH)$_4^-$ monomer,
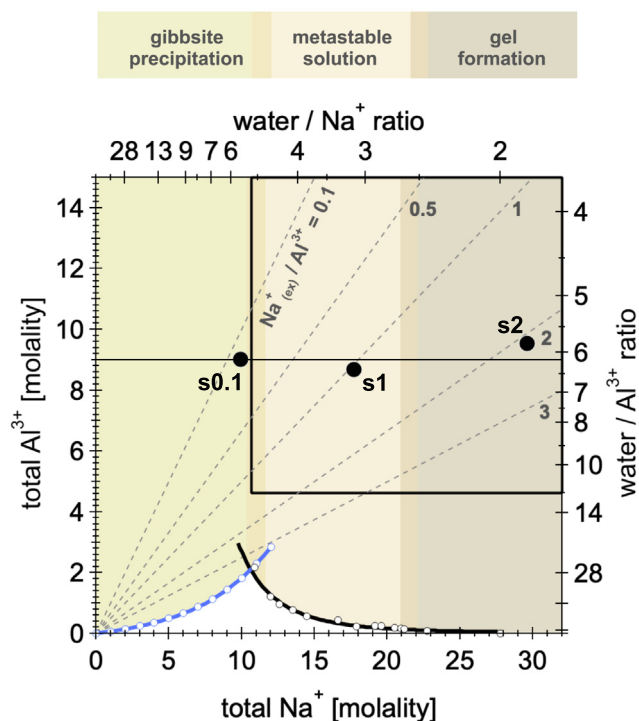

Fig. 1. Phase diagram of the sodium aluminate solutions at 25–30 °C. Solution compositions within this diagram show variability in metastability toward precipitation and their respective precipitation pathways. Gibbsite and sodium aluminate salt solubility curves are shown by the thick blue and black lines, respectively [33–38]. The maximum solubility is near 2 m [Al^{3+}]$_{tot}$ and 10 m [Na$^+$]$_{tot}$. The dashed diagonal lines follow constant Na$^+_{(ex)}$/Al^{3+} ratios of 0.1, 0.5, 1, 2, and 3. Solutions falling within the grey square boundary do not have enough water molecules to fully solvate all solute species and are considered to be "water-in-salt" solutions. Phase diagram is modified from Wang et al. [5] with copyright permission from American Chemical Society.

the μ$_2$-oxo Al$_2$O(OH)$_6^{2-}$ dimer [9–11,15,39,40], and possibly the di-μ$_2$-hydroxo Al$_2$(OH)$_8^{2-}$ dimer [11]. Raman and FTIR spectroscopy provide direct information about aluminate speciation and have been used here to determine the role of speciation in a solution's stability towards precipitation. Raman spectra of protiated aluminate solutions show three intense features that can be attributed to aluminate speciation: ~535 cm^{-1}, ~620 cm^{-1}, and ~705 cm^{-1} [8,10,11,15,41]. The band observed at ~620 cm^{-1} is assigned to the symmetric ν$_s$ AlO$_4$ stretching of the tetrahedral Al(OH)$_4^-$ unit [8,10,11,15,41]. The bands at ~535 and 705 cm^{-1} [8,10,11,15,41] and are assigned to the symmetric ν$_s$ Al-μO stretching and stretching vibrations of ν Al-ηO in the μ$_2$-oxo Al$_2$O(OH)$_6^{2-}$ molecule [8,10,11,15,41] (the notation of η represents non-bridging oxygen atoms, and ηO is essentially the oxygen of terminal hydroxyls). Raman bands corresponding to ν Al-μO and ν Al-ηO vibrations in the di-μ$_2$-hydroxo Al$_2$(OH)$_8^{2-}$ dimer are broadly predicted at ~608 cm^{-1}, which overlaps with the Al(OH)$_4^-$ band at ~620 cm^{-1} [9,11]. Due to overlapping vibrational features for the di-μ$_2$-hydroxo Al$_2$(OH)$_8^{2-}$ dimeric species and the fact that the Raman spectral range between 400 and 850 cm^{-1} can be modeled with assuming just the Al(OH)$_4^-$ monomer and the Al$_2$O(OH)$_6^{2-}$ dimer [11,14], the contribution of Al$_2$(OH)$_8^{2-}$ dimeric species is not resolvable using Raman data alone.

In the deuterated system, the ~620 cm^{-1} band for ν$_s$ AlO$_4$ mode is shifted to ~600 cm^{-1}, and the ~705 cm^{-1} band for ν Al-ηO modes is shifted to ~730 cm^{-1} [10,15,42]. The band at 535 cm^{-1} for the ν$_s$ Al-μO mode is approximately the same in both protiated and deuterated solutions as it does not directly involve H/D [15,41]. Fig. 2a shows that the Raman spectra for the solutions studied here contain all three features. The ν$_s$ Al-μO mode, occurring at 530.5 cm^{-1}, is slightly lower than the reported literature value and is constant across the concentration series (Fig. 2a). The ν$_s$ AlO$_4$ mode shifts from 603.0 to 608.6 cm^{-1} as the [Na$^+$] increases (Fig. 2a). The ν Al-ηO mode shifts from 717.6 to 714.2 with increasing [Na$^+$] (Fig. 2a). Changes in peak positions or intensities due to the H/D isotopic effects, or to an increase in concentration, reflect a change in the aluminate ion bonding environment, including contributions from Al-O-H/D bending, variations in the H/D-bond strength and the role of ion pair interactions [43,44]. The shift in the peak for the ν$_s$ AlO$_4$ mode of the Al(OH)$_4^-$ monomer indicates a change in its local environment, potentially affecting the energetics associated with dimerization. Because of the impact of H/D substitution on the ν Al-ηO mode, the peak shift observed with increasing [Na$^+$] reveals an alteration of deuterium (hydrogen) bonding (See Fig. S1 and Table S1 for detailed band analysis).

By neglecting the presence of Al$_2$(OD)$_8^{2-}$, the other two species (Al(OD)$_4^-$ and Al$_2$O(OD)$_6^{2-}$) that mainly give rise to Raman bands in the 400–850 cm^{-1} region have almost equal molar scattering coefficients [14]. This means that the relative peak areas in the 400–850 cm^{-1} region can be used to estimate their relative populations in these solutions [14,45]. In the s0.1 solution (Fig. 2a-b and S1b), the predominant species is Al(OD)$_4^-$, but Al$_2$O(OD)$_6^{2-}$ represents approximately one third of the population. At higher [NaOD]$_{tot}$ concentrations, the intensity of the monomeric peak (ν$_s$ AlO$_4$) decreases while the intensity of the two dimeric side bands (ν Al-ηO and ν$_s$ Al-μO) increases. This indicates that Al$_2$O(OD)$_6^{2-}$ is formed at the expense of Al(OD)$_4^-$, since there is a near-constant concentration of [Al^{3+}]$_{tot}$ across the solution series (Fig. 2-a-b). In the s2 solution, the predominant solution species is Al$_2$O(OD)$_6^{2-}$, because the overall intensity of the 535 + 715 cm^{-1} bands exceeds that of the monomeric band (Fig. 2a-b and S1d).

Because the [Al^{3+}]$_{tot}$ is fixed in these three solutions (~9 m), the formation of either one of the dimer species (or higher-order oligomers) must occur at the expense of monomers in the s1 and s2 solutions (Fig. 2b). The 400 to 850 cm^{-1} region of Raman spectrum for the s1 solution can be fit with a linear combination of the spec-
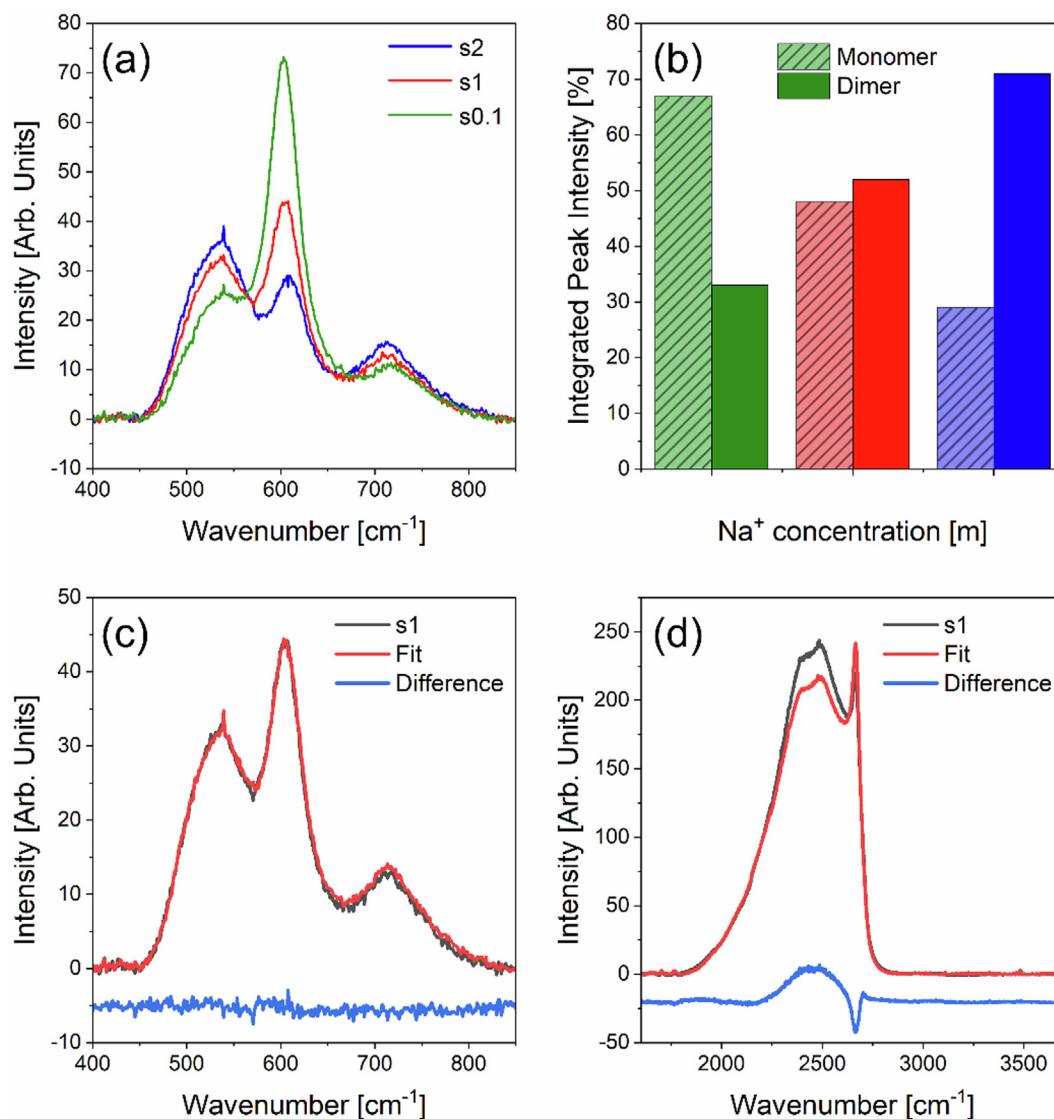
Fig. 2. (a) Background subtracted Raman spectra of the s0.1, s1, s2 solutions. In the 400–850 cm^{-1} region, the ν_s AlO$_4$ mode for the Al(OD)$_4^-$ monomer is centered at ~605 cm^{-1} and the ν_s Al-μO and ν Al-ηO modes in the Al$_2$O(OD)$_6^{2-}$ aluminate dimer are the two side bands at ~535 cm^{-1} and ~715 cm^{-1}. The full spectral range is given in the Figure S1a. (b) The relative abundance of Al(OD)$_4^-$ monomer and Al$_2$O(OD)$_6^{2-}$ dimer based upon the 605 cm^{-1} peak area and the combined 535 cm^{-1} and 715 cm^{-1} peak areas relative to the total area from 400 to 850 cm^{-1}, respectively. Fitting with Voigt line shapes was used to determine peak areas and fits are shown in in Figure S1b-d. (c) Fitting of the aluminate bands of the s1 spectrum using a linear combination of the s0.1 (36%) and s2 solution spectra (64%). (d) Fitting of the O-D stretch region of the s1 spectrum using a linear combination of the s0.1 (36%) and s2 solution spectra (64%).

tra for the s2 and s0.1 endmember compositions to give 36 % s0.1 and 64 % s2 (Fig. 2c). This suggests that s1 does not contain any spectroscopically unique solution species that are not present in either s0.1 or s2; thus, the enhanced metastability of s1 is not due to the presence of a new aluminate solution species. In contrast, the 1600–3000 cm^{-1} region of the Raman spectrum for the s1 solution, which corresponds O-D stretching vibrations (Fig. 2d), cannot be fit using a linear combination of s0.1 and s2 solution spectra, indicating that the interactions of D$_2$O and OD$^-$ may be key to the metastability of this solution.

FTIR spectroscopy provides additional insight into aluminate speciation by probing well-defined intramolecular vibrations that are characteristic of the bonding atoms, and can be used in combination with Raman spectroscopy to overcome issues associated with overlapping peaks. The primary IR band of the Al(OH)$_4^-$ monomer is at ~720 cm^{-1}, and is assigned to antisymmetric ν_{as} AlO$_4$ stretching vibrations. The characteristic IR bands of the μ$_2$-oxo Al$_2$O(OH)$_6^{2-}$ dimer are at ~550 (weak), 690, 880, and 928 cm^{-1}

[9–11], where the last two bands (~880 and 928 cm^{-1}) form a broad ~880–928 cm^{-1} absorption peak. These features are used to identify the presence of the μ$_2$-oxo Al$_2$O(OH)$_6^{2-}$ dimer species in solution. The IR bands of the di-μ$_2$-hydroxo Al$_2$(OH)$_8^{2-}$ dimer are predicted to overlap with the IR features of the Al$_2$O(OH)$_6^{2-}$ species, with the exception of an intense absorption peak at ~550 cm^{-1}, compared to the weak shoulder in the overlapping μ$_2$-oxo Al$_2$O(OH)$_6^{2-}$ IR band [9,11].

The IR spectra for the s0.1, s1 and s2 solutions are shown in Fig. 3 with emphasis on the aluminate region; full spectra are in Figure S2. With increasing [NaOD]$_{tot}$, the main peak shifts from 709 cm^{-1} to 703 cm^{-1} and decreases in intensity. This peak is mainly due to the ν_{as} AlO$_4$ mode in the Al(OD)$_4^-$ monomer, but the aluminate dimers also have signals in this region. The intensity of the broad peak centered at ~885 cm^{-1} increases with concentration from s0.1 to s2. This peak is characteristic of the μ$_2$-oxo Al$_2$O(OD)$_6^{2-}$ dimer, but the Al$_2$(OD)$_8^{2-}$ dimer also has some weak intensity in this region. A small feature that varies from 610 cm^{-1} in the
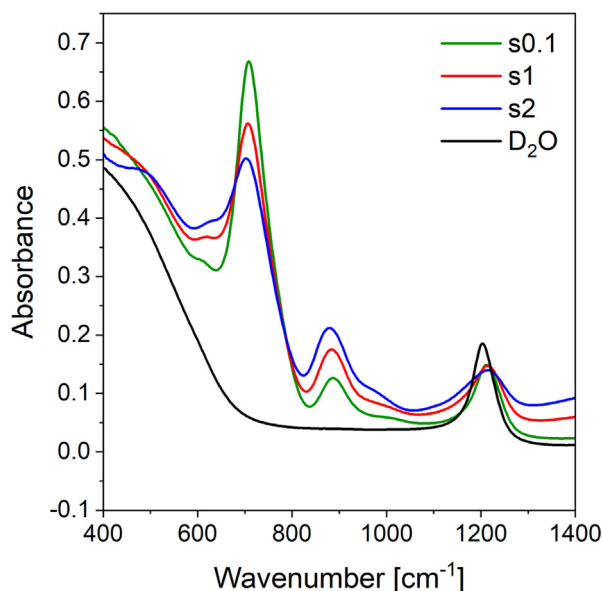
Fig. 3. FTIR spectra of the s0.1, s1 and s2 solutions, and a reference of bulk D_2O. The full spectral range is given in Figure S2.

s0.1 to 628 cm^{-1} in the s2 (Fig. 3) has been previously reported [10], but not assigned to a specific aluminate species. Theoretical calculations [11] suggest that this weak feature may arise from the ν_s AlO$_4$ mode (in Al(OD)$_4^-$) which becomes IR-active due to the induced charge delocalization by ion pairing interactions or by a slight change in the molecular symmetry. An additional feature at ~500 cm^{-1} appears with increasing [NaOD]$_{tot}$ and is most intense in the s2 solution. This feature could indicate the presence of the di-μ_2-deuteroxo Al$_2$(OD)$_8^{2-}$ dimer. However, if this species is present in appreciable amounts and with a long-enough lifetime to be detected and resolved, the ~605 cm^{-1} band in the Raman spectrum for the s2 solution should be broader and shifted to lower wavenumbers, which is not observed. Instead, it is likely that this feature at ~500 cm^{-1} is associated with ion pair interactions

involving the μ_2-oxo Al$_2$O(OD)$_6^{2-}$ dimer [11] that become more prevalent in the s2 solution. From the vibrational spectroscopies, the Al(OD)$_4^-$ monomer and μ_2-oxo Al$_2$O(OD)$_6^{2-}$ dimer appear to be the only aluminate solution species, both of which are tetrahedrally coordinated; there is no evidence for resolved alternative aluminate coordination states in solution.

3.3. Nuclear magnetic resonance spectroscopy

NMR spectroscopy was used to interrogate the coordination of Al^{3+} and Na$^+$, as well as the mobility of protons in the s0.1, s1, and s2 solutions. The ^{27}Al NMR spectra are shown in Fig. 4a. ^{27}Al is a spin 5/2 nucleus, and the chemical shift of the resonance is sensitive to the coordination of Al^{3+}. In solution, the chemical shifts for Al^{3+} in tetrahedral, pentahedral, and octahedral coordination are at ~80 ppm, ~35 ppm, and ~0 ppm, respectively [46]. Fig. 4a shows that only a single ^{27}Al NMR resonance is observed for all solutions, despite the evidence for the presence of multiple tetrahedrally-coordinated species in the Raman/IR spectra. This indicates that the chemically-distinct tetrahedrally-coordinated aluminate ions (i.e., the Al(OD)$_4^-$ monomer and the Al$_2$O(OD)$_6^{2-}$ dimer) are undergoing chemical exchange reactions that are fast relative to the NMR timescale, and thus a single ensemble peak is observed [47].

The peak maximum of the ^{27}Al resonance (Fig. 4a) is located at ~80 ppm, but changes as a function of solution composition from ~80 ppm in s0.1 to 73.6 in s2. This change in chemical shift of the ^{27}Al resonance is possibly attributed to: (i) changes in species concentration, with the peak position more weighted to monomeric species in s0.1 and to dimeric (or higher-order oligomeric) species in s2; (ii) OD ligand dynamics [48] and changes with H/D substitution [44]; and (iii) ion pairing of the various aluminate species. The full width half maximum (FWHM) of the ^{27}Al resonance does not increase monotonically with [Na$^+$]$_{tot}$ concentration, and this could be due to the chemical exchange between the Al(OD)$_4^-$ monomer and Al$_2$O(OD)$_6^{2-}$ dimer shown in Raman/IR spectroscopy. The end members, s0.1 and s2, contain predominantly Al(OD)$_4^-$ and Al$_2$O (OD)$_6^{2-}$, respectively (Fig. 2b) and have a narrower FWHM than the s1 solution with intermediate [Na$^+$]$_{tot}$ concentration, which contains a near equivalent mixture of Al(OD)$_4^-$ and Al$_2$O(OD)$_6^{2-}$.
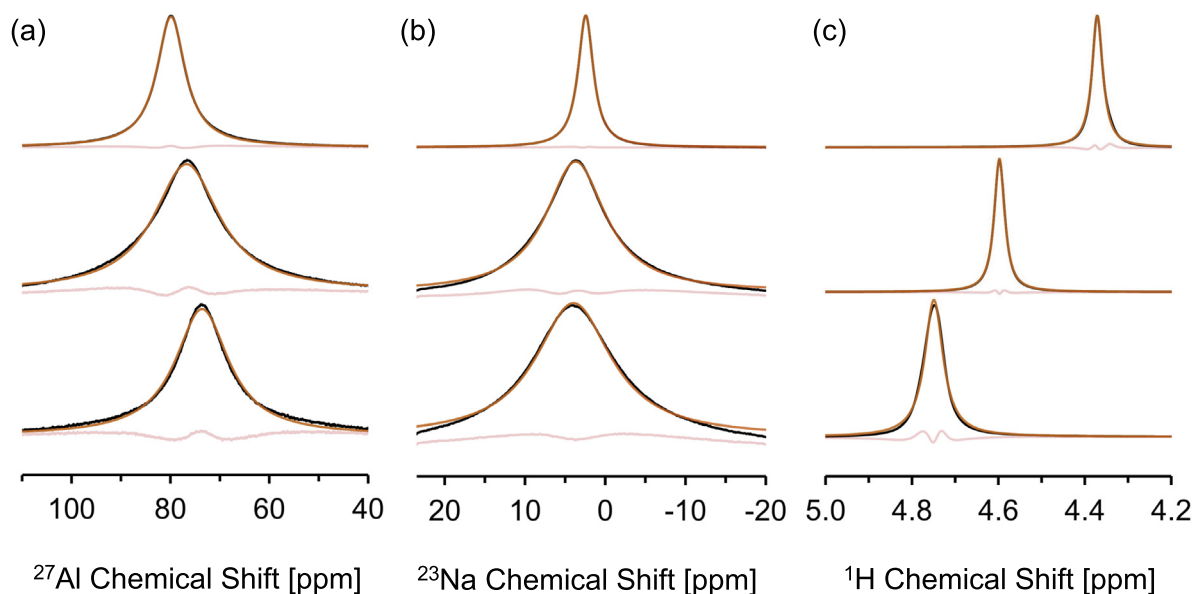

Fig. 4. NMR spectroscopy at 11.7 T. The (a) ^{27}Al NMR spectra, (b) ^{23}Na NMR spectra and (c) ^{1}H NMR spectra are shown for the s0.1 (top), s1 (middle) and s2 (bottom) solutions. The data were fit to a purely Lorentzian line shape, shown in orange and the residual between the fit and the data is shown in red. Note that spectra are normalized by their maximum peak height. The fitting results are tabulated in Table S2.
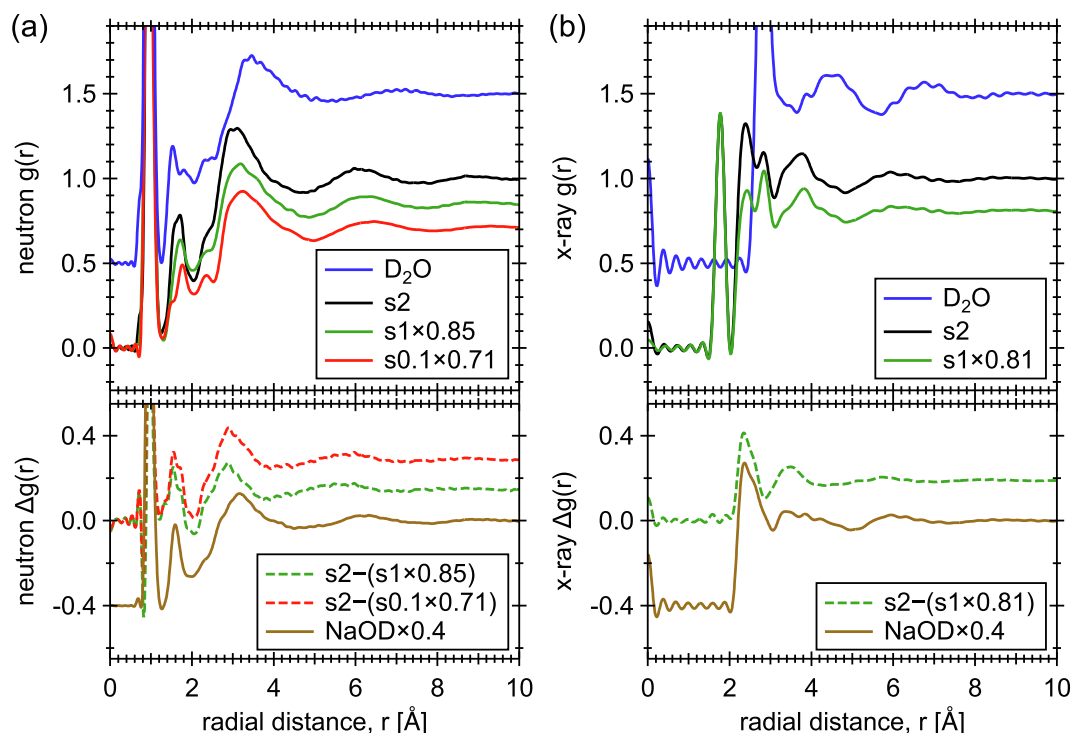
Fig. 5. Measured (a) neutron and (b) X-ray RDF g(r) patterns for structure of pure water (D$_2$O), three deuterated sodium aluminate solutions (s2, s1, and s0.1), and sodium deuteroxide solution (18 m NaOD). The D$_2$O RDF is offset by +0.5 in the y-axis for clarity. The difference RDF △g(r) patterns are plotted in the bottom panel together with the scaled NaOD solution data (offset by −0.4 in the y-axis) for ease of comparison. The NaOD RDF data is adopted from our previous work [23].

The ^{23}Na NMR spectra for the solutions also show a single resonance at all compositions (Fig. 4b). The increase in Na$^+$ chemical shift with concentration in the s0.1, s1, and s2 solutions agrees with the trend for Na$^+$ in NaOH solutions [49]. The FWHM of the ^{23}Na resonance also increases with increasing [Na$^+$]$_{tot}$ (Fig. 4b), which is distinct from the trend observed in the ^{27}Al NMR spectra (Fig. 4a).

^{1}H NMR spectroscopy was performed to interrogate the properties of the residual (<1%) H in the deuterated solutions. Only a single ^{1}H resonance was observed for all solutions, which indicates that chemical exchange of ^{1}H between H$_2$O, OH$^-$ and aluminate species is fast relative to the NMR timescale (Fig. 4c). The single ^{1}H resonance is consistent with previous studies on protonated sodium and potassium aluminate solutions [6,7]. The chemical shift of the ensemble resonance increased as the [Na$^+$]$_{tot}$ increased (Fig. 4c). In the ^{1}H diffusion measurements (Table S2), the diffusion of protons decreased from $0.712 \pm 0.027 \times 10^{-10}$ m^{2}s^{-1} in s0.1, to $0.212 \pm 0.005 \times 10^{-10}$ m^{2}s^{-1} in s1, to 0.074×10^{-10} m^{2}s^{-1} in s2. Using the ^{1}H diffusion coefficient of water ($D_w = 20.3 \times 10^{-10}$ m^{2}s^{-1} [50]) and the viscosity of water ($\eta_w = 1$ centipoise (cp) at 20 °C), the viscosity of the solutions can be estimated via $\eta_i = \eta_w \cdot (D_w/D_i)$, where η is the viscosity, D is the diffusion coefficient, and the subscripts w and i denote water molecules and solution species of interest. This approximation leads to estimated viscosities of 30 cp for s0.1, 100 cp for s1, and 270 cp for s2. This viscosity approximation neglects the contribution of other H-bearing species such as dissolved aluminate and hydroxide on the measured diffusion coefficient. Additionally, deuterium substitution results in deuterated solutions becoming more viscous than their protiated equivalents [51,52]. As a consequence of the high solution viscosities and isotope-dependent NMR properties (relaxation properties and gyromagnetic ratio [16,53,54]), ^{23}Na and ^{27}Al diffusion measurements via PFGSTE NMR were not possible in these concentrated solutions.

3.4. Experimental neutron and X-ray radial distribution functions

The complementary features of neutron and X-ray RDFs g(r) for the deuterated solution series are shown in Fig. 5. Both neutron and X-ray RDFs probe the well-defined intramolecular Al-OD and OD-OD bonding geometries in the aluminate anions. Because the RDF data is self-normalized, i.e., the limit g(r → ∞) = 1, neutron RDFs of the s0.1 and s1 solutions are multiplied by a weighting factor of 0.71 and 0.85, respectively, for a proper comparison. This scales the two g(r) curves relative to the s2 solution data (Fig. 5a), according to the expected scattering weights of the intramolecular Al-O$_a$ pair contributions (O$_a$ = oxygen sites of an aluminate ion). The weighting factors are calculated based on [Al^{3+}]$_{tot}$ (Table 2, see Supplementary Material, section 6, for details). For the X-ray RDFs, a factor of 0.81 is applied to the s1 solution data, which scales the intensity of the 1.80(5) Å peak for the Al-O$_a$ bonds in the s1 solution relative to the s2 solution data (Fig. 5b). The direct difference RDFs △g(r) between the scaled (s0.1 and s1) and unscaled (s2) solution data (Fig. 5) represent the residual signals that contain the pair-wise correlations involving Na$^+$ and OD$^-$ ions (e.g., Na-OD, Na-D$_2$O, OD-D$_2$O, Na-aluminate, and OD-aluminate). These three △g(r) curves are similar to the RDF data for concentrated (18 m) NaOD solutions [23] (Fig. 5; bottom panel). The similarity of the two △g(r) curves in the neutron data suggests that RDF analysis may not be sensitive to the change of aluminate speciation from monomers to dimers oligomers in these solutions (Fig. 1), but yet there are some trends across the series.

Two peaks that can be readily interpreted are: (i) the 0.97(5) Å intramolecular (covalent) O-D bonds in D$_2$O, OD$^-$ and aluminate ions in the neutron data, and (ii) the 1.80(5) Å Al-O$_a$ bonds within an aluminate ion in the X-ray data (Fig. 5). These two correlations are well-separated peaks in the corresponding neutron or X-ray RDFs. At distances of 1.3–2 Å, the broadening and shifting of the doublet peaks in the neutron RDFs correspond to changes in H/

Table 2
Neutron scattering weights (as %) of pair-wise partial contributions for the three sodium aluminate solutions studied.

Pairs	if alum. = $Al(OD)_4^-$ or $Al_2(OD)_8^{2-}$			if alum. = $Al_2O(OD)_6^{2-}$		
	s0.1	s1	s2	s0.1	s1	s2
1: Na-Na	0.05	0.14	0.31	0.06	0.16	0.34
2: Na-OD_{ex}	0.03	0.50	1.44	0.04	0.55	1.59
3: Na-D_2O	3.02	4.71	6.13	3.38	5.20	6.76
4: Na-alum.	1.37	2.05	2.94	1.25	1.86	2.65
5: OD_{ex}-alum.	0.42	3.59	6.84	0.39	3.26	6.18
6: OD_{ex}-D_2O	0.94	8.23	14.29	1.05	9.10	15.74
7: OD_{ex}-OD_{ex}	0.005	0.44	1.68	0.01	0.48	1.85
8: alum.-alum.	9.14	7.41	6.95	6.88	5.52	5.16
9: alum.-D_2O	40.39	33.98	29.06	37.05	30.82	26.27
10: D_2O-D_2O	44.64	38.94	30.35	49.90	43.05	33.45

D-bonding interactions, due to the increasing [OD⁻] from s0.1 to s2 (Fig. 5a). These changes are not due to the shortening of Al-O$_a$ distances, as the corresponding ~1.80(5) Å peaks in the X-ray RDF nearly coincide between the s1 and s2 solutions (Fig. 5b). Instead, the leading source of variations seen in Fig. 5a (at 1.3–2 Å) arise from the strong H/D-bonding interaction between the deuteroxide-O$_d$ and water-D$_w$ sites (O$_d$···D$_w$), which are normally 0.3–0.4 Å shorter than H/D-bond lengths between O$_w$···D$_w$ in pure water (typically at ~1.85 Å). At distances > 2 Å, neutron RDFs are difficult to assign because the pair-wise correlations between different species overlap and combine into a single measured g(r) pattern. In contrast to the neutron data, the X-ray scattering is insensitive to H/D substitution and is more sensitive to the other elements in the solutions. The X-ray RDFs clearly show two separated peaks at ~2.4 and ~2.85 Å and a broad correlation centered at ~3.5 Å (Fig. 5b). According to previous work [20], the ~2.4 Å peak is composed of contributions from three Na···O correlations, where the first-neighboring O is either from water-O$_w$ sites (for Na⁺ solvation) or from deuteroxide-O$_d$ or aluminate-O$_a$ sites (for contact ion pair formation). The ~2.85 Å peak is composed of a first-neighboring shell of O$_w$···O$_w$, O$_d$···O$_w$ and O$_a$···O$_w$ correlations, with the latter two of these arising from the OD⁻ and aluminate ion solvation, as well as from the intramolecular O$_a$-O$_a$ and Al-Al bonding geometries within an aluminate ion. These Al-Al correlations only exist in the aluminate dimers or higher-order oligomers. The broad g(r) signals at ~3.5 Å in the X-ray RDFs arise from the second-neighboring shell of O$_w$···O$_w$ and O$_d$···O$_w$, and the first-neighboring shell of Al···O$_w$ and Al···Na correlations. Increasing [Na⁺]$_{tot}$ from s0.1 to s2 visibly shifted the RDF g(r) oscillations (at > 3 Å) to shorter distances, as compared to the pure water RDF, including the second-shell of O$_w$···O$_w$ and O$_d$···O$_w$. This salt effect leading to a more compact, high-density ion-water/water-water network (Fig. 5) [23,49,55] is in a manner analogous to pure water under elevated pressure [23,56–61]. The second shell D$_w$···O$_w$ and D$_w$···D$_w$ correlations, in contrast, only broaden and shift slightly to shorter distances with increasing [Na⁺]$_{tot}$ due to reorientational disorder [23,60,61]. The ion-induced D$_w$-D$_w$ RDF is highly variable between different molecular simulation protocols (see examples in [23,55]). The D$_w$-O$_w$ and D$_w$-D$_w$ RDFs are best probed by neutron total scattering, while the O$_w$-O$_w$ RDF is best seen by X-ray total scattering.

3.5. Geometric models of solvated species

Geometric modeling, rather than a complete solution structure simulation, was performed with the solute species involved to understand the short-range features of the experimental RDF (see more discussion in Supplementary Material, section 7). In the simplest scenario, each ion (cation or anion) is fully surrounded by water molecules in the first solvation shell, i.e., ion pairing is not considered. The first solvation shell (FSS) geometry of a given type of ion configured from AIMD simulations is shown in Fig. 6. For aluminate ions (monomer or dimers), the aluminate OH ligands are both H-bond donors and acceptors, and can take two to three H-bonds from nearby water molecules. On average, there are 10–12 H$_2$O around an Al(OH)$_4^-$ ion in the FSS, and each H$_2$O interacts via a single H-bond to the OH ligands (Fig. 6a). The average number of H$_2$O in the FSS around the two dimers is 14–18, but they show a larger variation in solvation shell size and H-bonding characteristics. For instance, some H$_2$O molecules are shared by two OH ligands, or in between the OH ligand and μ$_2$-OH (or μ$_2$-O) sites, forming a bidentate configuration (Fig. 6b-c). The FSS environments around OH⁻ ions follow the literature [23,55,62–64], where OH⁻ accepts three to four H-bonds from H$_2$O (O$_h$···H$_w$) and weakly donates one to another H$_2$O (H$_h$···O$_w$), i.e., 4–5 H$_2$O in FSS (Fig. 6d). The solvation structures around Na⁺ ions also agree with literature data [65–70], with Na···O$_w$ distances (~2.3–2.6 Å) smaller than the O$_w$···O$_w$ distances (~2.85 Å) of pure water, and 5–6 H$_2$O in FSS for a fully hydrated Na⁺ ion (Fig. 6e).

In each solvated molecular motif, three characteristic partial structure correlations can be defined for ion-water and water-water interactions. They are partial RDFs of: (i) the intramolecular site-site geometry of the central ion, (ii) the intermolecular correlations between the central ion and the surrounding water molecules, and (iii) the water-water correlations within and beyond the first solvation shell (Fig. 7). For a Na⁺ ion, the RDF of the intramolecular partial term is zero. For other anions, the intramolecular RDFs are essentially self-correlation g(r) functions, since there is only one anion in a sea of water per simulation box (Fig. 7a). The intermolecular ion-water RDFs reflect structural aspects of ionic hydration shells (Fig. 7b). The water-water RDFs include the primary intramolecular geometry of a water molecule and the intermolecular water-water interactions (Fig. 7c). The latter is related to ionic perturbation of the local water structuring, but these ion-induced changes are not significant due to the infinite dilution in the AIMD simulations. The complete neutron and X-ray partial RDFs computed from the solvated molecular motifs are shown in Figures S3 and S4 (in Supplementary Material, section 8).

Distinguishing between the monomeric and dimeric structural motifs is difficult due to their similar RDFs (Fig. 7a). However, since water solvation structure around the Al(OD)$_4^-$ monomer features only monodentate D-bonding coordination (Fig. 6a), the distribution of D-bond lengths (1.8 ± 0.1 Å) in the monomer's FSS is narrower than those observed for the dimers (1.8 ± 0.3 Å; Fig. 7b). This feature corresponding to water molecules interacting with Al(OD)$_4^-$ is well-separated from the 1.55(2) Å D$_w$···D$_w$ intramolecular distance within a water molecule (Fig. 7c) and from the strong 1.50(5) Å D-bonding interactions between the deuteroxide-O$_d$ and water-D$_w$ sites (O$_d$···D$_w$; Fig. S3d).

Geometric modeling is based on nonlinear least-squares methods, in which the theoretical structure functions (pair-wise corre-
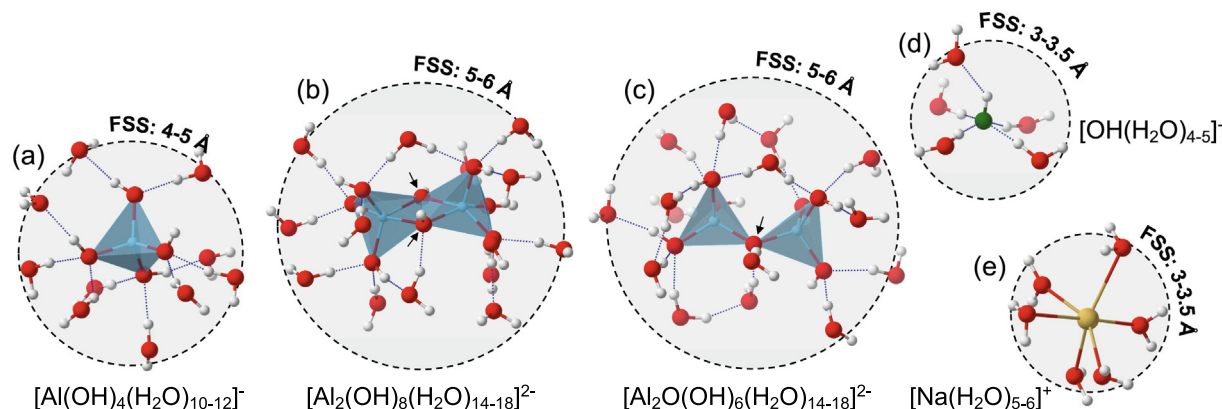
Fig. 6. Snapshots from the AIMD simulations of the fully solvated structure of (a) $Al(OH)_4^-$ monomer, (b) di-μ_2-hydroxo $Al_2(OH)_8^{2-}$ dimer, (c) μ_2-oxo $Al_2O(OH)_6^{2-}$ dimer, (d) OH^-, and (e) Na^+. The circle encapsulates the first solvation shell (FSS), which defines the molecular motifs used to generate the partial RDFs presented in Figures 7, S3 and S4. O atoms are shown as red spheres, H as white spheres, Al as blue polyhedra, hydroxide-O as green sphere, and Na as yellow sphere. The H-bonds are shown as blue dotted lines. The arrows indicate the bridging μ_2-hydroxo (μ_2-OH) or μ_2-oxo (μ_2-O) sites in the two dimeric species.
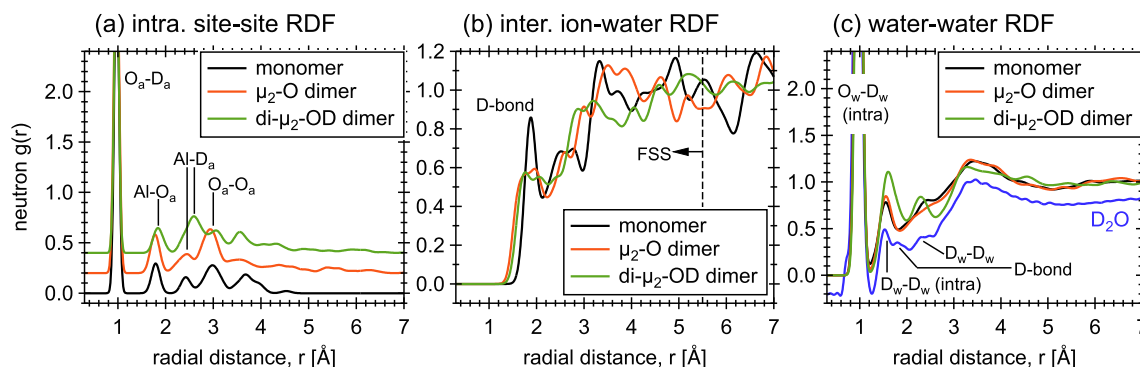
Fig. 7. Calculated neutron partial RDFs of the solvated aluminate anion motifs illustrated in Fig. 6. (a) intramolecular site-site RDFs, (b) intermolecular ion-water RDFs, and (c) water-water RDFs. Peaks that are readily identified are labelled. In the plot a, the intramolecular site-site correlations within each aluminate anion are stacked (by +0.2 in the y-axis) for clarity. In the plot c, the RDF of the experimental pure D_2O data is presented (and offset by −0.2 in the y-axis) for ease of comparison to the computed water-water correlations within and beyond the first solvation shell in each molecular motif model. Note that all the computed partial RDFs were self-normalized and generated on the basis of deuterated species, i.e. D_2O, $Al(OD)_4^-$ (monomer), $Al_2O(OD)_6^{2-}$ (μ_2-O dimer), and $Al_2(OD)_8^{2-}$ (di-μ_2-OD dimer).

lations) are calculated in the reciprocal Q-space with adjustable structural parameters and geometrical rules [20]. The theoretical structure functions are then compared with experiment to achieve the best fit. The adjustable structural parameters and geometrical rules comprise the bond distances, the Debye-Waller terms, and the concentration or coordination numbers. For instance, aluminate ions in monomeric or dimeric forms have well-defined polyhedral shapes, with tetrahedral geometry in $Al(OD)_4^-$ and $Al_2O(OD)_6^{2-}$, and pentahedral geometry in $Al_2(OD)_8^{2-}$. The distance correlations in aluminate ions ($Al-O_a$, $Al-D_a$, O_a-O_a, O_a-D_a, D_a-D_a and $Al-Al$), and their Debye-Waller terms, can be calculated/refined on the basis of the geometrical constraints, and the resulting structure function is commonly known as the intramolecular scattering form factor [71]. The hydration structure of the aluminate ions, in contrast, takes the relevant distances (e.g., $Al \cdots O_w$, $O_a \cdots O_w$, $D_a \cdots O_w$, etc.), and coordination numbers as free parameters with no regular geometry assumed, and the associated Debye-Waller factors are typically larger. For these solutions, a large number of structural parameters is required to achieve even a rough estimation of local structure correlations for all the solute species involved, see example in [20].

Here, the solvated molecular motifs used in the geometric models are from AIMD simulations (Fig. 6), with no refinements to the hydration structure or hydration numbers. This simulation-informed approach provides an alternate way to interpret local sol-

vent–solute structure contributions to the experimental neutron and X-ray RDFs. To scale the relative contribution of partial RDFs from the defined molecular motifs, the scattering weights for each pair-wised partial were calculated. The neutron-weighted coefficients of deuterated pair-wise contributions to the overall scattering of the solutions are given in Table 2 (for details, see Supplementary Material, section 6). During RDF data analysis, these weighting coefficients were used to decide which pair-wise interactions had a significant effect on the overall observed intensity. For the three solutions, different aluminate speciation is assumed, with all Al^{3+} ions present in solution as either: (i) the $Al(OD)_4^-$ monomer; (ii) the di-μ_2-deuteroxo $Al_2(OD)_8^{2-}$; or (iii) the μ_2-oxo $Al_2O(OD)_6^{2-}$ dimer. The $Al(OD)_4^-$ and $Al_2(OD)_8^{2-}$ aluminate ions are composed of the same stoichiometry and the total Al^{3+} concentration in solution is equivalent, thus, the weighting coefficients for these species are identical, but their intramolecular and solvation structural functions are not the same (Fig. 7). Vibrational spectroscopy and NMR have shown that the relative abundance of the three species in s0.1, s1 and s2 is between that of pure $Al(OD)_4^-$ and pure $Al_2O(OD)_6^{2-}$, with a possible presence of $Al_2(OD)_8^{2-}$. Higher-order tetrahedrally coordinated aluminate oligomers may also be present, but they likely have similar local structures to the $Al_2O(OD)_6^{2-}$ dimer.

About 85–87% of the measured neutron intensities in s0.1 comprises contributions from aluminate solvation (37–40%) and ion-

induced water-water correlations (45–50%) (Table 2). At r < 5 Å, there are additional 7–9% contributions from the intramolecular correlation of an aluminate ion (monomer or dimer; see Fig. 7a). Together, these three partials (no. 8–10 in Table 2) contribute up to ~94% of the total measured intensity in s0.1. Note that Na^+ and OD^- solvation signals (no. 3 and 6 in Table 2) only contribute ~4% of the total intensity. In solutions with excess $[Na^+]_{tot}$ relative to $[Al^{3+}]_{tot}$, the solvation contributions from Na^+ and OD^- ions become more significant (s1 and s2 in Table 2), although no. 8–10 partial weights still dominate. In all solutions, the weights of the cation–anion correlations such as $Na-OD_{ex}$ and Na-aluminate, are quite small (no more than ~3%; no. 2 and 4 in Table 2), and contribute weakly to the total intensity of neutron RDFs. Because the prevalent O and D atoms in aqueous solutions scatter neutrons as strongly as the Na and Al atoms, the scattering weights of O- and D-containing solute or solvent species dominate the overall features of neutron RDF patterns.

Fig. 8 shows a comparison of experimental and calculated neutron RDFs from the various geometric model protocols. The complete model (brown dashed lines in Fig. 8) for each aluminate species comprises the linear combination of partial RDFs, including aluminate solvation (plus the aluminate's intramolecular term), OD^- solvation (plus the covalent intramolecular O_d-D_d bond), Na^+ solvation, and water-water correlations, all weighted by the expected % contributions. The water-water RDFs are adopted from the water structuring in solvated aluminate models (either monomer, di-μ_2-deuteroxo dimer, or μ_2-oxo dimer). Similar results can also be achieved when using water-water RDFs from the solvated sodium or deuteroxide models, as these water-water RDFs behave similarly to the structure of pure water (Fig. 7c, S3 and S4). However, the water-water structuring around the di-μ_2-deuteroxo dimer is more ordered, which leads to the well-shaped 2.3 Å peak (assigned to the first shell coordination of intermolecular $D_w \cdots D_w$) and a series of distinct minima presented in the water-water RDFs (Fig. 7c and 8d-f).

All three geometric models differ in various regions when compared to the experimental neutron RDFs. The monomer speciation model captures the relative RDF peak intensities and positions for the s0.1 data, whereas the two dimeric models describe the RDF patterns equally well in the s1 and s2 data. These observations are limited to the short-r range distances (r < 5 Å), where aluminate solvation and water-water correlations are mainly from the first solvation shell network and/or from the near-neighboring distances. Agreements between the models and experimental neutron data suggest that the local aluminate bonding environment does not deviate significantly from the fully solvated structural configuration. For ions to maintain their solvation shell at high $[Na^+]_{tot}$, solvent-shared ion pairs (SSIPs) are likely formed by distortion of the nearest neighbor water structure.

From the traditional concept of size-over-charge for the ions, the first solvation shell of Na^+ and OD^- ions are stronger in bonded interactions with water molecules than the aluminate-water H/D-bonds since they are smaller ions, but of the same charge. The strength of the interactions in latter can be inferred to be competitive to the water-water H/D-bonding in pure water because of the similar H/D-bond lengths. Water molecules play an important role in controlling the activation energy for ion association reactions to form SSIPs, where, for example, one or two water molecules coordinate to Na^+ and donate H-bonds to aluminate anion. In pure concentrated/saturated NaOD (NaOH) aqueous solutions, Na^+ is still able to retain its weak selectivity towards water molecules despite the deficiency of solvent water molecules [55,72]. For instance, Na^+ coordinates on average to 0–2 OH^- and 4–5 H_2O molecules, with total coordination numbers ranging from 4 to 7 at saturation (27.7 m) [72]. The RDFs for water molecules solvated around OH^- also do not change significantly as a function of concentration,

and only decrease slightly in numbers of coordinating water (but not its structure) [64,73]. These observations suggest that at high NaOD (NaOH) concentrations, ions are predominantly present as water-bridged pair complexes, forming ion-water networks regardless of the sign of the ions' charge [23,72,73]. The specific bonded interactions of H-bonds between OH^- and H_2O can drive formation of anionic pair structures (composed of two OH^- bridged by two or three water molecules), where the increased Coulombic repulsion within these anionic pair structures is compensated locally by the presence of nearby cations [73].

We postulate a similar reaction mechanism for SSIP formation in the present concentrated sodium aluminate solutions, where SSIP species may not be limited to cation–anion pairs at high $[Na^+]_{tot}$. Anion-anion SSIPs, assisted by H-bonding interactions and charge compensated by nearby cations, become increasing important because aluminate polymerization reactions must begin with H-bond formation between OH ligands of two separate $Al(OH)_4^-$ anions. Contact ion pair (CIP) formation is expected as the solution becomes a "water-in-salt" condition (i.e., deficient in water molecules; Fig. 1). For the Na^+ and $Al(OH)_4^-$ cation–anion interactions, potential of mean force calculations (in dilute conditions) show that the free energy barrier to convert between SSIP and CIP is quite small (~1–1.3 kcal/mole [12]), suggesting a kinetically labile cation–anion association reaction. The $Al(OH)_4^-$-Na^+ CIP was 0.1 to 0.4 kcal/mole more stable than the $Al(OH)_4^- \cdots Na^+$ SSIP, which implies a coexistence of these two types of ion pairs. The formation of CIP in the first solvation shell of aluminate and OD^- anions will replace one or two first-shell water molecules when Na^+ is monovalently coordinated to the O_a or O_d sites. At very high concentrations, more Na^+ could be expected in the first solvation shell through clustering of the aluminate species [74].

The same modeling analysis of the X-ray RDFs does not agree as well with the experimental spectra as the neutron RDFs do (Fig. 9; see also Fig. S5 for a complete comparison). This discrepancy is largely due to the elemental sensitivity differences between neutron and X-ray total scattering. In the concentrated sodium aluminate solution system, neutron total scattering is sensitive to changes in H/D-bonding interactions by ion solvation. X-ray scattering is highly insensitive to H/D atoms, and hence, ion-pairing interactions contribute more (~15–21%) to the total intensity (Table S3). Quantifying the fractions of contact or water-shared ion pair structures, and determining the presence of larger cation–anion ion clusters for the Na-aluminate ($Na \cdots O_a$, $Na \cdots D_a$, $Na \cdots Al$) and Na-OD ($Na \cdots O_d$, $Na \cdots D_d$) interactions, are difficult with geometric models because the contact ion-pair distances of $Na \cdots O_a$ and $Na \cdots O_d$ overlap with the $Na \cdots O_w$ distances, i.e., they all occurred at ~2.4 Å. Significant changes to the O_w-O_w RDF due to densification of the water network with increasing $[Na^+]_{tot}$ are not captured in the geometric solvation models, so peak intensities at ~2.4 Å and ~3.5 Å correlation features in the experimental X-ray RDF are not reproduced by the model RDF (Fig. 9). Additional ion-ion correlations for $Na \cdots Na$ (~3–4 Å [75]) and $Na \cdots Al$ (~3.8 Å for CIPs [12]) are also not included in the simple geometric model, and likely contribute to intensity mismatches at ~3.5 Å in the X-ray RDFs, suggesting that CIPs may be present in these highly concentrated solutions.

3.6. Molecular mechanisms controlling aluminate solution reactions

Solution-phase reactions are controlled by ion coordination changes, therefore, inner-sphere H_2O and OH^- ligands around Na^+ and Al^{3+} ions must determine the reactivity of the ionic complexes (structural motifs) in these concentrated sodium aluminate solutions. H_2O and OH^- are the most abundant species and actively participate in proton transfer through H-bonding interactions. The elementary reactions of (de)protonation and ion association with
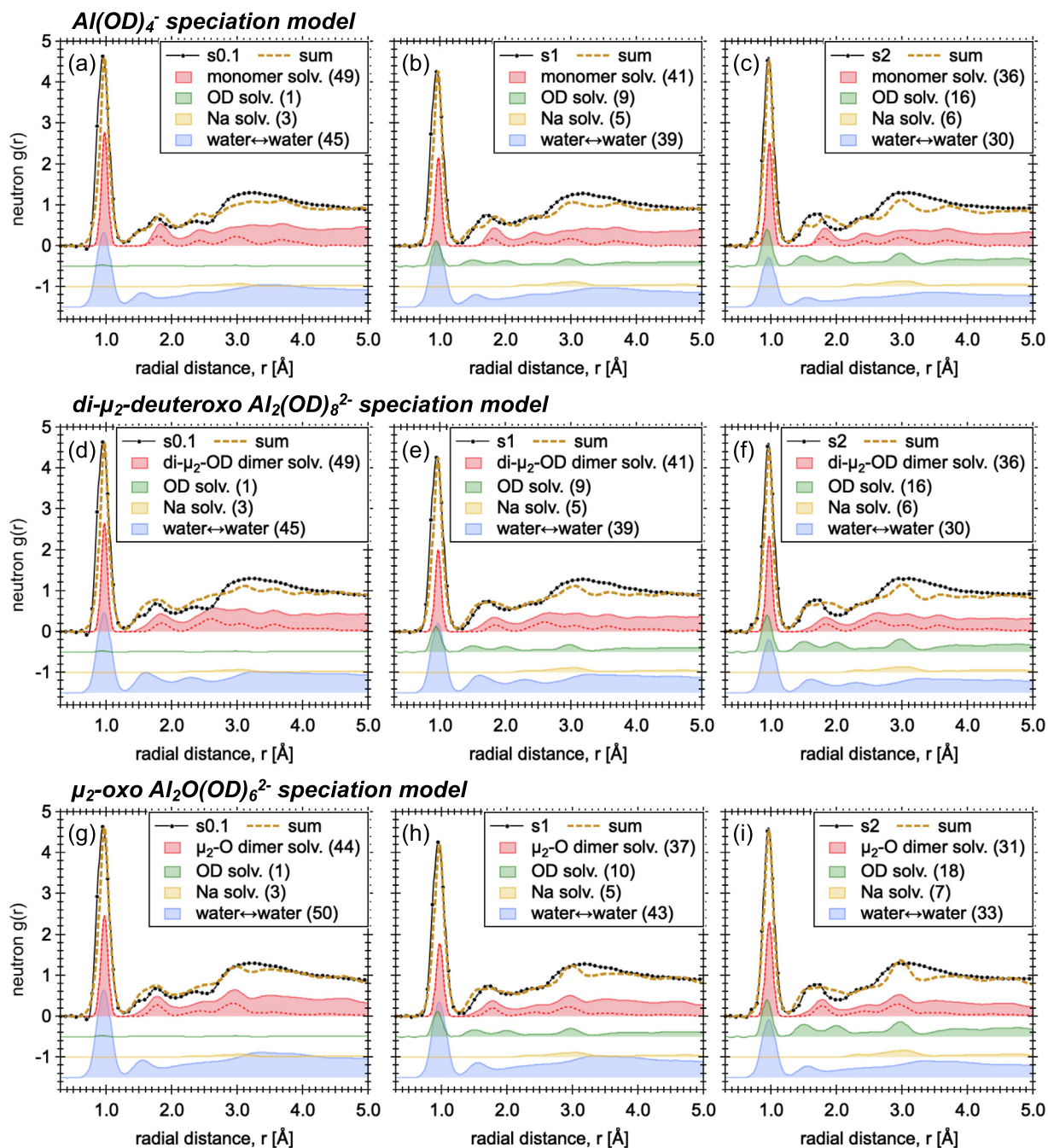
Fig. 8. Measured neutron RDF g(r) patterns (bold black curves) compared to RDFs (brown dashed curves) obtained from various geometric models for s0.1 (a, d, g), s1 (b, e, h), and s2 (c, f, i) solution data. The simulated total RDFs (brown dashed curve) are composed of contributions of aluminate anion solvation (plus the aluminate's intramolecular term; red), OD⁻ solvation (plus the covalent intramolecular O_d-D_d bond; green), Na⁺ solvation (yellow), and water-water (blue) correlations. The intramolecular site-site bonding correlation within an aluminate ion is illustrated by red dashed curves. Three different aluminate speciation cases are presented for each studied solution. The number in parentheses for each partial RDF represents the weighting contribution (%) to the total observed intensity (see Table 2).

different types of coordinated oxygens must govern aluminate solution reactivity and metastable zones. Although a comprehensive molecular understanding of the reaction mechanisms remains elusive, several general phenomena can be inferred, based on the results presented here and our previous studies, within the context of the phase diagram (Fig. 1).

The scattering and spectroscopy results show that the population of dimers and/or oligomers increases with increasing $[Na^+]_{tot}$, in this study, and/or $[Al^{3+}]_{tot}$, consistent with previous studies [8,10,14,41]. Mechanistically, hydroxyl-containing moieties (either OH⁻ ions or OH ligands) are critical for polymerization as they

facilitate H-bonding and promote proton transfer. DFT cluster calculations and MD analysis of $Al(OH)_4^-$ dimerization revealed that, because of the strong ability of $Al(OH)_4^-$ to retain its hydroxylic protons, the formation of dimeric complexes begins with H-bonded interactions between the two $Al(OH)_4^-$ anions (Scheme 1), which are sufficient to compensate the electrostatic repulsion between the two negatively charged hydroxocomplexes [12,76]. According to Scheme 1, simulations performed under dilute conditions predict that the energy of formation of ≡Al-(OH)₂-Al≡ vs. ≡Al-O-Al≡ links (where ≡ represent three aluminate-OH ligands) found in the di-μ₂-hydroxo $Al_2(OH)_8^{2-}$ and μ₂-oxo $Al_2O(OH)_6^{2-}$

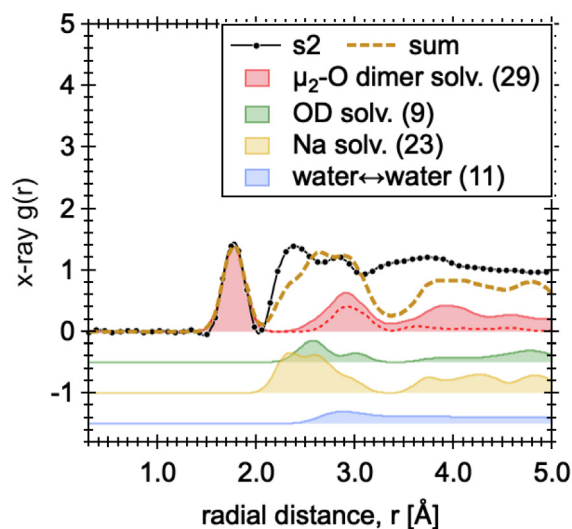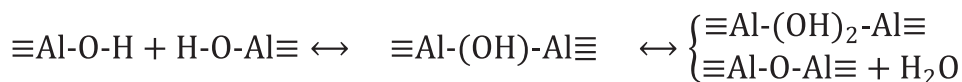### μ_2-oxo $Al_2O(OD)_6^{2-}$ speciation model

Fig. 9. Measured X-ray RDF g(r) pattern (bold black curve) compared to RDF (brown dashed curve) obtained from various geometric models for the s2 solution data. The simulated total RDF (brown dashed curve) is composed of contributions of aluminate anion solvation (plus the aluminate's intramolecular term; red), OD^- solvation (plus the covalent intramolecular O_d-D_d bond; green), Na^+ solvation (yellow), and water-water (blue) correlations. Only the s2 solution data and the $Al_2O(OD)_6^{2-}$ speciation case are presented here (for others see Fig. S5). The number in parentheses for each partial RDF represents the weighting contribution (%) to the total observed intensity (Table S3). Note the missing simulation intensities at ~2.4 and ~3.5 Å relative to the experimental data.

dimers, respectively, differs only slightly under fully solvated conditions [76]. Formation of the di-μ_2-hydroxo $Al_2(OH)_8^{2-}$ dimer from the intermediate species of a singly hydroxo-bridged $\equiv$Al-(OH)-Al$\equiv$ configuration (i.e., the μ_2-hydroxo $Al_2(OH)_8^{2-}$) is kinetically favorable, with a reaction barrier smaller than ~3 kcal/mole due to the simple reorientation/bridging of the aluminate-OH ligands [12]. The μ_2-oxo $Al_2O(OH)_6^{2-}$ dimer is thermodynamically more favored (by ~6.4 to 7.9 kcal/mole [12,76]) with respect to the $Al_2(-OH)_8^{2-}$ dimer, but its formation from the same intermediate species involves the transfer of the proton and consequently requires overcoming a higher energy barrier of ~7.5 kcal/mole [12]. When CIPs form between Na^+ and either of the two dimers, the $Al_2O(OH)_6^{2-}$-Na^+ species is also energetically favored by ~3.4–7.1 kcal/mole [12]). However, in dilute solutions, the stabilizing effect of Na^+ on the dimerization reaction pathway is predicted to be minor, i.e., CIP interactions do not necessary decrease the dimerization energies when compared to simple water solvation without a counter cation [12]. Under high $[Na^+]_{tot}$ and $[Al^{3+}]_{tot}$ conditions, where competition for water molecules occurs, there is a thermodynamic driving force for ionic cluster formation consisting of a hydrogen (deuterium) bonded polyhedral network [23,72,73]. The energetic difference between the monomer and the two dimers within this network may be inverted. The transition from $Al_2(OH)_8^{2-}$ to $Al_2O(OH)_6^{2-}$, which releases H_2O, would be favorable in the absence of solvating waters, and when the counter cations are involved in a variety of SSIP coordination states other than CIPs.

Atomistic simulations at elevated concentrations are required to determine the mechanisms of aluminate complexation and polymerization reactions in these ion networks.

The reactivity of different coordinated oxygens generally varies *inversely* with their coordination numbers whenever the bridging bonds between two mental cation centers are formed or destroyed [77]. In the solvated $Al(OH)_4^-$ hydroxocomplexes, all four oxygens are nonbridging oxygens (the η-OH sites) exposed to solution, and are key active sites for reactions. Fully solvated $Na(H_2O)_{5-6}^+$ has five to six nonbridging η-OH_2 sites for water (inter)exchange reactions. The $Al_2(OH)_8^{2-}$ dimer has six nonbridging η-OH sites and two bridging μ_2-OH sites, while the $Al_2O(OH)_6^{2-}$ dimer has six nonbridging η-OH sites and one bridging μ_2-O site. Although, both dimeric complexes have the same number of nonbridging η-OH sites, their relative reactivity is affected by the type and number of bridging sites, i.e., the doubly μ_2-OH in $Al_2(OH)_8^{2-}$ vs. the singly μ_2-O in $Al_2O(OH)_6^{2-}$. The formation of the μ_2-O site involves deprotonation of the μ_2-OH bridges to form μ_2-O$\cdots$(H-OH)$\cdots\eta$-OH (where the two -OH are from the nearby η-OH sites), and the release of the weakly bound H_2O molecule from the μ_2-O site [12]. This suggests that the μ_2-O site is less susceptible to (re)protonation and has more electronegativity than the μ_2-OH sites, thereby favoring ion-pairing interactions between the μ_2-O site and Na^+ [12]. The formation of $Al_2O(OH)_6^{2-}$ dimer may become more favorable at high $[Na^+]_{tot}$, where ion-pair interactions could both stabilize this form of the dimer, and promote growth of larger oligomers with the μ_2-oxo-type linkage. However, protonation of the μ_2-OH bridge in the singly or doubly hydroxo-bridged $Al_2(-OH)_8^{2-}$ species by nearby H_2O or OH^- would form μ_2-OH_2, which is a much weaker bridge, and lead to the dissociation of $Al_2(OH)_8^{2-}$ dimers. While this research suggests that H-bonding and proton transfer reactions with key bridging hydroxyls play a significant role in the formation of $\equiv$Al-(OH)$_2$-Al$\equiv$ versus $\equiv$Al-O-Al$\equiv$ links during polymerization, the reaction mechanism is further complicated by the participation of excess OH^-, free H_2O molecules, and specific cations in the formation of oligomeric species.

Characterization of the dynamic properties of H_2O, OH^-, and aluminate, and their local cooperative motions using quasielastic neutron scattering and ^1H NMR spectroscopy show a significant slowing of water diffusion, and greater local or confined motions, for ionic complexes formed at elevated concentrations of $[Na^+]_{tot}$ and $[Al^{3+}]_{tot}$ [6,7]. Inelastic neutron scattering investigations [78] also suggest a strengthening of the H-bonding network with increasing $[Na^+]_{tot}$ and $[Al^{3+}]_{tot}$. ^1H NMR studies on the trace amounts of H present in the deuterated solutions in this study show that H diffusion is decreased as $[Na^+]_{tot}$ is increased while $[Al^{3+}]_{tot}$ is held constant. Together, these microscopic dynamic processes are connected to the reactivity of ionic complexes and to crystallization behaviors. As $[Na^+]_{tot}$ and $[Al^{3+}]_{tot}$ increases, extended ion clustering or aggregation in the ion-water network can induce geometric frustration, effectively inhibiting nucleation by providing a free-energy barrier to the structural reorganization needed for crystallization. In addition, the structure of these larger μ_2-oxo-bridged aluminate oligomers in solution may not correspond to the structure or stoichiometry of the equilibrium bulk crystals, so they would not fulfil the role of the molecular scale building blocks required for nucleation processes. The larger oligomers also consist of a high ratio of bridging μ_2-O sites (per Al site),

$$\equiv\text{Al-O-H} + \text{H-O-Al}\equiv \;\longleftrightarrow\; \equiv\text{Al-(OH)-Al}\equiv \;\longleftrightarrow\; \begin{cases} \equiv\text{Al-(OH)}_2\text{-Al}\equiv \\ \equiv\text{Al-O-Al}\equiv + \text{H}_2\text{O} \end{cases}$$

Scheme 1. Mechanism of the $Al(OH)_4^-$ dimerization in alkaline solutions to generate the two principal dimeric species, di-μ_2-hydroxo $Al_2(OH)_8^{2-}$ and μ_2-oxo $Al_2O(OH)_6^{2-}$. Both dimers form from the intermediate species of μ_2-hydroxo $Al_2(OH)_8^{2-}$ (with a single hydroxo-bridge). The triple and quadruple bar symbols represent the aluminate-OH ligands. The depicted mechanism is based on the AIMD studies by Pouvreau et al. [12] and Jin et al. [76].

so would not be as active as the smaller monomers or dimers composed of a high ratio of nonbridging η-OH and bridging μ₂-OH sites. Thus, these larger oxo-bridged oligomers may hinder nucleation reactions and be slow-releasing reservoirs for the reactive small monomers and dimers. Similar arguments for the large cage-like and cyclic solute species that are much less reactive than monomers, or small, acyclic aluminosilicate oligomers have been observed in the formation of aluminosilicate minerals (e.g., zeolite) from alkaline solutions [77].

4. Conclusions

The challenges associated with resolving aluminate speciation in the alkaline sodium aluminate system using spectroscopic and scattering techniques include: (i) overlapping characteristic vibrational bands for the monomer and the two dimers in Raman/IR spectroscopy; (ii) fast chemical exchange reactions between tetrahedral coordinated aluminates resulting in a single ^{27}Al NMR resonance frequency; and (iii) uncertainty in distinguishing between the monomeric and the two dimeric structural motifs in RDF analysis. However, results presented here, in the context of previous investigations, show that hydrogen (deuterium) bonding and proton (deuterium) transfer control aluminate speciation and chemical reactivity in concentrated alkaline aluminate solutions. Metastability and nucleation processes in these supersaturated solutions depend on $[Al^{3+}]_{tot}$, excess OH^-, water activity, and the nature of the cation. As $[Na^+]_{tot}$ and/or $[Al^{3+}]_{tot}$ increases, the aluminate species change from monomers to dimers/oligomers due to competition for water molecules, enhanced H-bonding, and proton transfer reactions. The solvation of these complex entities and the nature of oligomeric bridging configurations influence dynamics, chemical reactivity, and ultimately precipitation behaviors observed in these alkaline aluminate solutions. This improved understanding of the concentrated alkaline aluminate solution system may provide a stronger fundamental basis for development of models meant to predict conditions leading to precipitation, such as in radioactive tank waste processing and industrial aluminum production. Future work using ultrafast spectroscopy techniques supported with computational molecular simulations could be valuable for exploring relationships between proton transfer and aluminate complexation reactions.

Declaration of Competing Interest

The authors declare that they have no known competing financial interests or personal relationships that could have appeared to influence the work reported in this paper.

Appendix A. Supplementary data

Supplementary data to this article can be found online at https://doi.org/10.1016/j.molliq.2022.120379.

References

[1] A.T. Tabereaux, R.D. Peterson, Aluminum production, in: S. Seetharaman (Ed.), Treatise on Process Metallurgy, Elsevier, Boston, 2014, pp. 839–917.
[2] A.R. Hind, S.K. Bhargava, S.C. Grocott, The surface chemistry of Bayer process solids: A review, Colloids Surf. A 146 (1-3) (1999) 359–374.
[3] H.A. Colburn, R.A. Peterson, A history of Hanford tank waste, implications for waste treatment, and disposal, Environ. Prog. Sustain. Energy 40 (2020) e13567.
[4] S.B. Clark, M. Buchanan, B. Wilmarth, Pacific Northwest National Lab.(PNNL), Richland, WA (United States), 2016.
[5] H.-W. Wang, K. Yuan, N. Rampal, A.G. Stack, Solution and interface structure and dynamics in geochemistry: Gateway to link elementary processes to mineral nucleation and growth, Cryst. Growth Des. 22 (2021) 853–870.
[6] T.R. Graham, D. Semrouni, E. Mamontov, A.J. Ramirez-Cuesta, K. Page, A. Clark, G.K. Schenter, C.I. Pearce, A.G. Stack, H.-W. Wang, Coupled multimodal dynamics of hydrogen-containing ion networks in water-deficient, sodium hydroxide-aluminate solutions, J. Phys. Chem. B 122 (50) (2018) 12097–12106.
[7] H.-W. Wang, T.R. Graham, E. Mamontov, K. Page, A.G. Stack, C.I. Pearce, Countercations control local specific bonding interactions and nucleation mechanisms in concentrated water-in-salt solutions, J. Phys. Chem. Lett. 10 (12) (2019) 3318–3325.
[8] H.R. Watling, P.M. Sipos, L. Byrne, G.T. Hefter, P.M. May, Raman, IR, and ^{27}Al-MAS-NMR spectroscopic studies of sodium (hydroxy)aluminates, Appl. Spectrosc. 53 (4) (1999) 415–422.
[9] M. Dembowski, M.P. Prange, M. Pouvreau, T.R. Graham, M.E. Bowden, A. N'Diaye, G.K. Schenter, S.B. Clark, A.E. Clark, K.M. Rosso, C.I. Pearce, Inference of principal species in caustic aluminate solutions through solid-state spectroscopic characterization, Dalton Trans. 49 (18) (2020) 5869–5880.
[10] R.J. Moolenaar, J.C. Evans, L.D. McKeever, Structure of the aluminate ion in solutions at high pH, J. Phys. Chem. 74 (20) (1970) 3629–3636.
[11] M. Pouvreau, M. Dembowski, S.B. Clark, J.G. Reynolds, K.M. Rosso, G.K. Schenter, C.I. Pearce, A.E. Clark, Ab initio molecular dynamics reveal spectroscopic siblings and ion pairing as new challenges for elucidating prenucleation aluminum speciation, J. Phys. Chem. B 122 (29) (2018) 7394–7402.
[12] M. Pouvreau, E. Martinez-Baez, M. Dembowski, C.I. Pearce, G.K. Schenter, K.M. Rosso, A.E. Clark, Mechanisms of Al^{3+} dimerization in alkaline solutions, Inorg. Chem. 59 (24) (2020) 18181–18189.
[13] J.W. Akitt, W. Gessner, Aluminium-27 nuclear magnetic resonance investigations of highly alkaline aluminate solutions, J. Chem. Soc., Dalton Trans (1984) 147–148.
[14] P. Sipos, P.M. May, G. Hefter, Quantitative determination of an aluminate dimer in concentrated alkaline aluminate solutions by Raman spectroscopy, Dalton Trans. (2) (2006) 368–375.
[15] P. Sipos, The structure of Al(III) in strongly alkaline aluminate solutions — A review, J. Mol. Liq. 146 (1-2) (2009) 1–14.
[16] T.R. Graham, K.S. Han, M. Dembowski, A.J. Krzysko, X. Zhang, J. Hu, S.B. Clark, A. E. Clark, G.K. Schenter, C.I. Pearce, K.M. Rosso, ^{27}Al pulsed field gradient, diffusion-NMR spectroscopy of solvation dynamics and ion pairing in alkaline aluminate solutions, J. Phys. Chem. B 122 (48) (2018) 10907–10912.
[17] P. Sipos, G. Hefter, P.M. May, ^{27}Al NMR and Raman spectroscopic studies of alkaline aluminate solutions with extremely high caustic content–Does the octahedral species $Al(OH)_6^{3-}$ exist in solution, Talanta 70 (4) (2006) 761–765.
[18] L. Barcza, M. Pálfalvi-Rózsahegyi, The aluminate lye as a system of equilibria, Mater. Chem. Phys. 21 (4) (1989) 345–356.
[19] A. Buvari-Barcza, M. Rózsahegyi, L. Barcza, Hydrogen bonded associates in the Bayer process (in concentrated aluminate lyes): the mechanism of gibbsite nucleation, J. Mater. Chem. 8 (1998) 451–455.
[20] T. Radnai, P.M. May, G.T. Hefter, P. Sipos, Structure of aqueous sodium aluminate solutions: A solution X-ray diffraction study, J. Phys. Chem. A 102 (1998) 7841–7850.
[21] M. Wojdyr, Fityk: a general-purpose peak fitting program, J. Appl. Crystallogr. 43 (2010) 1126–1128.
[22] J. Neuefeind, M. Feygenson, J. Carruth, R. Hoffmann, K.K. Chipley, The nanoscale ordered materials diffractometer NOMAD at the spallation neutron source SNS, Nucl. Instrum. Methods Phys. Res., Sect. B 287 (2012) 68–75.
[23] D. Semrouni, H.-W. Wang, S.B. Clark, C.I. Pearce, K. Page, G. Schenter, D.J. Wesolowski, A.G. Stack, A.E. Clark, Resolving local configurational contributions to X-ray and neutron radial distribution functions within solutions of concentrated electrolytes – A case study of concentrated NaOH, Phys. Chem. Chem. Phys. 21 (13) (2019) 6828–6838.

[24] P.J. Chupas, X. Qiu, J.C. Hanson, P.L. Lee, C.P. Grey, S.J.L. Billinge, Rapid-acquisition pair distribution function (RA-PDF) analysis, J. Appl. Crystallogr. 36 (6) (2003) 1342–1347.

[25] I.S. Joung, T.E. Cheatham, Determination of alkali and halide monovalent ion parameters for use in explicitly solvated biomolecular simulations, J. Phys. Chem. B 112 (30) (2008) 9020–9041.

[26] P.B. Balbuena, K.P. Johnston, P.J. Rossky, Molecular dynamics dimulation of dlectrolyte dolutions in dmbient and dupercritical dater. 1. Ion solvation, J. Phys. Chem. 100 (1996) 2706–2715.

[27] J. Hutter, M. Iannuzzi, F. Schiffmann, J. VandeVondele, CP2K: Atomistic simulations of condensed matter systems, WIREs Comput. Mol. Sci. 4 (2014) 15–25.

[28] B. Hammer, L.B. Hansen, J.K. Nørskov, Improved adsorption energetics within density-functional theory using revised Perdew-Burke-Ernzerhof functionals, Phys. Rev. B 59 (11) (1999) 7413–7421.

[29] S. Grimme, J. Antony, S. Ehrlich, H. Krieg, A consistent and accurate ab initio parametrization of density functional dispersion correction (DFT-D) for the 94 elements H-Pu, J. Chem. Phys. 132 (2010) 154104.

[30] J. VandeVondele, M. Krack, F. Mohamed, M. Parrinello, T. Chassaing, J. Hutter, Quickstep: Fast and accurate density functional calculations using a mixed Gaussian and plane waves approach, Comput. Phys. Commun. 167 (2005) 103–128.

[31] J. VandeVondele, J. Hutter, Gaussian basis sets for accurate calculations on molecular systems in gas and condensed phases, J. Chem. Phys. 127 (2007) 114105.

[32] R.B. Neder, T. Proffen, Diffuse scattering and defect structure simulations: A cook book using the program DISCUS, Oxford University Press, 2008.

[33] T.R. Graham, R. Gorniak, M. Dembowski, X. Zhang, S.B. Clark, C.I. Pearce, A.E. Clark, K.M. Rosso, Solid-state recrystallization pathways of sodium aluminate hydroxy hydrates, Inorg. Chem. 59 (10) (2020) 6857–6865.

[34] Y. Zhang, S. Zheng, H. Du, S. Wang, Y.i. Zhang, Solubility of Al_2O_3 in the $Na_2O−Al_2O_3−H_2O−CH_3OH$ System at (30 and 60) °C, J. Chem. Eng. Data 55 (3) (2010) 1237–1240.

[35] H. Stephen, T. Stephen, Solubilities of inorganic and organic compounds, Pergamon Press, New York, 1965.

[36] T.R. Graham, M. Dembowski, E. Martinez-Baez, X. Zhang, N.R. Jaegers, J. Hu, M. S. Gruszkiewicz, H.-W. Wang, A.G. Stack, M.E. Bowden, C.H. Delegard, G.K. Schenter, A.E. Clark, S.B. Clark, A.R. Felmy, K.M. Rosso, C.I. Pearce, In situ ^{27}Al NMR spectroscopy of aluminate in sodium hydroxide solutions above and below saturation with respect to gibbsite, Inorg. Chem. 57 (19) (2018) 11864–11873.

[37] G. Qiu, N. Chen, Phase study of the system Na_2O-Al_2O_3-H_2O, Can. Metall. Q. 36 (1997) 111–114.

[38] J.W. Sprauer, D.W. Pearce, Equilibria in the Systems Na_2O–SiO_2–H_2O and Na_2O–Al_2O_3–H_2O at 25 °C, J. Phys. Chem. 44 (7) (1940) 909–916.

[39] C.T. Johnston, S.F. Agnew, J.R. Schoonover, J.W. Kenney 3rd, B. Page, J. Osborn, R. Corbin, Raman study of aluminum speciation in simulated alkaline nuclear waste, Environ. Sci. Technol. 36 (2002) 2451–2458.

[40] W. Rudolph, G. Hefter, Quantitative analysis in alkaline aluminate solutions by Raman spectroscopy, Anal. Methods 1 (2009) 132–138.

[41] H. Watling, Spectroscopy of concentrated codium aluminate solutions, Appl. Spectrosc. 52 (1998) 250–258.

[42] M.H. Brooker, P.R. Tremaine, Raman studies of hydration of hydroxy complexes and the effect on standard partial molar heat capacities, Geochim. Cosmochim. Acta 56 (6) (1992) 2573–2577.

[43] J.A. Tossell, Theoretical studies on aluminate and sodium aluminate species in models for aqueous solution: $Al(OH)_3$, $Al(OH)_4^-$, and $NaAl(OH)_4$, Am. Mineral. 84 (1999) 1641–1649.

[44] A.J. Krzysko, T.R. Graham, M. Dembowski, C. Beck, X. Zhang, K.M. Rosso, S.B. Clark, C.I. Pearce, Isotopic substitution reveals the importance of aluminate diffusion dynamics in gibbsite ($Al(OH)_3$) crystallization from alkaline aqueous solution, ACS Earth Space Chem. 6 (4) (2022) 999–1010.

[45] M. Dembowski, T.R. Graham, J.G. Reynolds, S.B. Clark, K.M. Rosso, C.I. Pearce, Influence of soluble oligomeric aluminum on precipitation in the Al-KOH-H_2O system, Phys. Chem. Chem. Phys. 22 (42) (2020) 24677–24685.

[46] M. Haouas, F. Taulelle, C. Martineau, Recent advances in application of ^{27}Al NMR spectroscopy to materials science, Prog. Nucl. Magn. Reson. Spectrosc. 94–95 (2016) 11–36.

[47] B.T. Poe, P.F. McMillan, B. Cote, D. Massiot, J.P. Coutures, Magnesium and calcium aluminate liquids: In situ high-temperature ^{27}Al NMR Spectroscopy, Science 259 (1993) 786–788.

[48] E. Martinez-Baez, R. Feng, C.I. Pearce, G.K. Schenter, A.E. Clark, Al 27 NMR chemical shift of $Al(OH)_4^{4-}$ calculated from first principles: Assessment of error cancellation in chemically distinct reference and target systems, J. Chem. Phys. 152 (2020) 134303.

[49] T.R. Graham, M. Dembowski, H.-W. Wang, S.T. Mergelsberg, E.T. Nienhuis, J.G. Reynolds, C.H. Delegard, Y. Wei, M. Snyder, I.I. Leavy, S.R. Baum, M.S. Fountain, S.B. Clark, K.M. Rosso, C.I. Pearce, Hydroxide promotes ion pairing in the $NaNO_2$–$NaOH$–H_2O system, Phys. Chem. Chem. Phys. 23 (1) (2021) 112–122.

[50] M. Holz, S.R. Heil, A. Sacco, Temperature-dependent self-diffusion coefficients of water and six selected molecular liquids for calibration in accurate ^1H NMR PFG measurements, Phys. Chem. Chem. Phys. 2 (2000) 4740–4742.

[51] J. Li, C.A. Prestidge, J. Addai-Mensah, Viscosity, density, and refractive index of aqueous sodium and potassium aluminate solutions, J. Chem. Eng. Data 45 (4) (2000) 665–671.

[52] P. Sipos, A. Stanley, S. Bevis, G. Hefter, P.M. May, Viscosities and densities of doncentrated aqueous $NaOH/NaAl(OH)_4$ mixtures at 25 °C, J. Chem. Eng. Data 46 (2001) 657–661.

[53] J. Mitchell, Can sodium NMR provide more than a tracer for brine in petrophysics, J. Pet. Sci. Eng. 146 (2016) 360–368.

[54] T.R. Graham, J. Chun, G.K. Schenter, X. Zhang, S.B. Clark, C.I. Pearce, K.M. Rosso, ^{27}Al NMR diffusometry of Al_{13} keggin nanoclusters, Magn. Reson. Chem. 60 (2) (2022) 226–238.

[55] T. Megyes, S. Balint, T. Grosz, T. Radnai, I. Bako, P. Sipos, The structure of aqueous sodium hydroxide solutions: a combined solution X-ray diffraction and simulation study, J. Chem. Phys. 128 (2008) 044501.

[56] A. Soper, The radial distribution functions of water and ice from 220 to 673 K and at pressures up to 400 MPa, Chem. Phys. Lett. 258 (2000) 121–137.

[57] S. Fanetti, M. Pagliai, M. Citroni, A. Lapini, S. Scandolo, R. Righini, R. Bini, Connecting the water phase diagram to the metastable domain: High-pressure studies in the supercooled regime, J. Phys. Chem. Lett. 5 (2014) 3804–3809.

[58] B. Chen, J.M. Park, I. Ivanov, G. Tabacchi, M.L. Klein, M. Parrinello, First-principles study of aqueous hydroxide solutions, J. Am. Chem. Soc. 124 (29) (2002) 8534–8535.

[59] S. Imberti, A. Botti, F. Bruni, G. Cappa, M.A. Ricci, A.K. Soper, Ions in water: the microscopic structure of concentrated hydroxide solutions, J. Chem. Phys. 122 (2005) 194509.

[60] J. Holzmann, R. Ludwig, A. Geiger, D. Paschek, Pressure and salt effects in simulated water: Two sides of the same coin, Angew. Chem. Int. Ed. Engl. 46 (46) (2007) 8907–8911.

[61] R. Mancinelli, A. Botti, F. Bruni, M. Ricci, A. Soper, Perturbation of water structure due to monovalent ions in solution, Phys. Chem. Chem. Phys. 9 (2007) 2959–2967.

[62] M.E. Tuckerman, D. Marx, M. Parrinello, The nature and transport mechanism of hydrated hydroxide ions in aqueous solution, Nature 417 (6892) (2002) 925–929.

[63] A. Botti, F. Bruni, S. Imberti, M.A. Ricci, A.K. Soper, Ions in water: The microscopic structure of a concentrated HCl solution, J. Chem. Phys. 121 (2004) 7840–7848.

[64] D. Marx, A. Chandra, M.E. Tuckerman, Aqueous basic solutions: hydroxide solvation, structural diffusion, and comparison to the hydrated proton, Chem. Rev. 110 (2010) 2174–2216.

[65] H. Ohtaki, T. Radnai, Structure and dynamics of hydrated ions, Chem. Rev. 93 (3) (1993) 1157–1204.

[66] S. Obst, H. Bradaczek, Molecular dynamics study of the structure and dynamics of the hydration shell of alkaline and alkaline-earth metal cations, J. Phys. Chem. 100 (39) (1996) 15677–15687.

[67] K.D. Collins, G.W. Neilson, J.E. Enderby, Ions in water: Characterizing the forces that control chemical processes and biological structure, J. Biol. Chem. 128 (2007) 95–104.

[68] J. Mähler, I. Persson, A study of the hydration of the alkali metal ions in aqueous solution, Inorg. Chem. 51 (1) (2012) 425–438.

[69] M. Kelley, A. Donley, S. Clark, A. Clark, Structure and dynamics of NaCl ion pairing in solutions of water and methanol, J. Phys. Chem. B 119 (51) (2015) 15652–15661.

[70] M. Galib, M.D. Baer, L.B. Skinner, C.J. Mundy, T. Huthwelker, G.K. Schenter, C.J. Benmore, N. Govind, J.L. Fulton, Revisiting the hydration structure of aqueous Na^+, J. Chem. Phys. 146 (2017) 084504.

[71] P. Egelstaff, An introduction to the liquid state, Elsevier, 2012.

[72] M. Hellström, J. Behler, Structure of aqueous NaOH solutions: insights from neural-network-based molecular dynamics simulations, Phys. Chem. Chem. Phys. 19 (2017) 82–96.

[73] I. Zadok, H. Long, B. Pivovar, A. Roznowska, A. Michalak, D.R. Dekel, S. Srebnik, Unexpected hydroxide ion structure and properties at low hydration, J. Mol. Liq. 313 (2020) 113485.

[74] H.R. Watling, S.D. Fleming, W. van Bronswijk, A.L. Rohl, Ionic structure in caustic aluminate solutions and the precipitation of gibbsite, J. Chem. Soc., Dalton Trans (1998) 3911–3918.

[75] A.P. Lyubartsev, A. Laaksonen, Concentration effects in aqueous NaCl solutions: A molecular dynamics simulation, J. Phys. Chem. 100 (1996) 16410–16418.

[76] X. Jin, R. Liao, T. Zhang, H. Li, Theoretical insights into the dimerization mechanism of aluminum species at two different pH conditions, Inorg. Chim. Acta 520 (2021) 120311.

[77] W.H. Casey, T.W. Swaddle, Why small? The use of small inorganic clusters to understand mineral surface and dissolution reactions in geochemistry, Rev. Geophys. 41 (2) (2003).

[78] M.P. Prange, T.R. Graham, R. Gorniak, M. Pouvreau, M. Dembowski, H.-W. Wang, L.L. Daemen, G.K. Schenter, M.E. Bowden, E.T. Nienhuis, K.M. Rosso, A.E. Clark, C.I. Pearce, Theory-guided inelastic neutron scattering of crystalline alkaline aluminate salts bearing principal motifs of solution-state species, Inorg. Chem. 60 (21) (2021) 16223–16232.